Supplementary Information for

Dissecting multilayer cell-cell communications with signaling feedback loops from spatial transcriptomics data

Table of Content

Supplementary References

Text S1. Collection and integration of prior network information

LigRecDB

The LigRecDB database in stMLnet collected the information from various databases including CellChat, connectomeDB, NicheNet and iTALK. These four databases stored information of interactions between ligands and receptors, which covered various data sources such as protein-protein interaction database, pathway database, gene regulatory database and literature-mining.

CellChat (Jin et al. 2021) collected four categories of ligand-receptor interaction information (interactions, complexes, co-effectors, and annotations) based on KEGG and literature-mining. By converting the interaction involving complexes into the interaction between molecules using the information from complexes, we obtained 1921 molecular interactions from CellChat, including 514 ligands and 439 receptors.

Based on Ramilowski et al. (Ramilowski et al. 2015), ConnectomeDB2020 (Hou et al. 2020) integrated databases embedded in several cell-cell communication tools, including CellphoneDB (Efremova et al. 2020), RNA-Magnet (Baccin et al. 2020), SingleCellSignalR (Cabello-Aguilar et al. 2020), ICELLNET (Noel et al. 2021), etc. All these ligand-receptor interactions are supported by literatures. We extracted 2293 pairs of ligand-receptor interactions from ConnectomeDB2020, involving 829 ligands and 690 receptors.

iTALK (Wang et al. 2019) was derived from text mining, categorizing ligand-receptor interactions into ‘checkpoint interaction’, ‘cytokine interaction’, ‘growth factor interaction’, and ‘other interaction’. To minimize information redundancy, we removed interactions coming from connectomeDB2020 and Ramilowski et al. database when utilizing iTALK. As a result, we obtained 2440 ligand-receptor interactions from iTALK, involving 692 ligands and 664 receptors.

NicheNet (Browaeys et al. 2020) gathered ligand-receptor interaction information from 14 data sources, including text mining, pathway databases, drug databases, and molecular interaction databases. When processing the data from NicheNet, we excluded some relatively unreliable ligand-receptor interactions. This included interactions sourced from the Ramilowski et al. database but were filtered in connectomeDB2020 as well as interactions predicted by NicheNet through molecular interaction database and GO database. From NicheNet, we screened out 2010 ligand-receptor interactions involving 536 ligands and 509 receptors.

We integrated the ligand-receptor interactions extracted from the above fours databases, retaining only those with HGNC gene correspondence. This yielded 3860 non-redundant ligand-receptor interactions, containing 972 ligands and 863 receptors. Additional details of these interactions were also recorded, for instance, the primary sources, the secondary sources, supporting literatures and occurrence times (**Fig S30A-B** and **Table S2**).

TFTGDB

The TFTGDB database in stMLnet collected interactions between transcriptional factors (TFs) and target genes (TGs) from TRRUST (Han et al. 2018), RegNetwork (Liu et al. 2015), HTRIdb (Bovolenta et al. 2012) and GTRD (Kolmykov et al. 2021).

TRRUST collected 9396 pairs of TF-TG interactions through literature mining, and labeled

specific regulatory relationships as 'activated', 'inhibited' and 'unknown'. After filtering miRNA interactions and contradictory regulator interactions, we ultimately preserved 8427 regulatory interactions.

RegNetwork was developed based on 25 databases, 17 of which provide regulatory relationship information and 8 of which are auxiliary databases. We downloaded regulatory interaction information from the RegNetwork website, filtered out miRNA-mediated and duplicate interactions, and finally retained 155426 pairs of regulatory interactions.

HTRIdb collected predicted and experimentally validated TF-TG interactions from classic regulatory databases such as JASPAR, TRANSFAC, TRED, and TRRD, as well as from relevant literatures. Using consistent filtering criteria (excluding miRNA-mediated interactions and repeated interactions), we obtained 18160 transcriptional regulatory interactions between 283 TFs and 11886 TGs.

GTRD interactive website was used to obtain regulatory binding sites near the transcription promoter. With the same filtering criteria (excluding miRNA-mediated interactions and repeated interactions), we identified 588238 pairs of TF-TG interactions involving 569 TFs and 6319 TGs.

Integrating the transcriptional regulation information extracted from the above four databases, we collected 754270 non-redundant TF-TG interactions, involving 1712 transcription factors and 23836 target genes. Additionally, we also recorded the following information for each interaction: primary data sources, secondary data sources, literature support information, and occurrence times (**Fig S31A-B** and **Table S2**).

RecTFDB

Receptor-transcription factor (TF) interactions are mainly collected from eight pathway-related databases by using R package graphite. For each pathway, we extracted component members and topological structure to construct three network modes: protein-protein interaction, metabolite-metabolite interaction, and protein-metabolite interaction. Based on the following rules, we obtained the interactions between protein molecules in the pathway using 'edges' function: (1) for complex complexes consisting of multiple protein molecules, interactions were assumed between each protein molecule; (2) for the metabolite-mediated interaction between two proteins (protein A→metabolite C→protein B), we reserved only interaction between proteins (protein A→protein B); (3) for the molecular interaction (A→B) of 'Process (Binding /association)' or 'undirected' type, we added the reverse interaction direction B→A. We extracted a total of 398809 non-redundant protein interactions involving 11354 proteins, consisting of 11354 proteins ranging from upstream regulatory molecules (ligands and receptors) to intermediate molecules (kinases, intermediates, etc.), and downstream molecules (transcription factors and target genes) (**Fig S30A-B** and **Table S2**). Among these proteins, there were 762 receptors acting on 1145 transcription factors.

Unlike direct interactions between ligand-receptor interactions or transcription factor-target interactions, regulations between receptors and transcription factors are typically transmitted indirectly through the assistance of multiple signal molecules. Moreover, the interaction information collected from the databases is usually incomplete and pathways involving crosstalk are frequently dispersed across different databases. For example, receptor a in

pathway A regulates intermediate signal molecule b (database 1), while intermediate signal molecule b in pathway B influences the activation of downstream transcription factor c (database 2). In this situation, by observing pathway A and pathway B separately, the regulatory potential between receptor a and downstream transcription factor c will be neglected. To resolve the above issues, we employed the pathway information of the above 8 databases to construct an integrated weighted directed graph to evaluate the regulatory potential between receptors and transcription factors. The direction was determined according to the direction of signal transmission, and the weight was determined according to the occurrence times of interactions in the databases. We assumed that receptor-transcription factor pairs with higher regulatory potential are closer to each other in the weighted directed graph than that with lower regulatory potential, and that the closer the distance is, the greater the potential of regulation (the distance is affected by the network topology and node attributes). In most cases, there is no direct connection between the receptor node and the transcription factor node. We can use the possibility of connection between two nodes to express the regulatory potential between the receptor and the transcription factor, which is analogy with the link prediction problem, so we use random walk with restart algorithm to predict receptor-transcription factor linking.

The sketch of the approach to constructing our RecTFDB database is as follows. We first constructed a weighted directed signal network with protein as node and interaction as edge. Each receptor was used as the starting point (seed node) for randomness. The receptor might return to itself with probability r (restart probability), or randomly wandered to nearby reachable nodes with 1-r probability. After multiple walks or resets, the probability of the receptor reaching to any other node in the graph would stabilize. As such, we obtained a probability matrix of 762 receptors regulating 1145 transcription factors, with each value in the matrix representing the potential of a pair of receptor-transcription factor interaction. These interactions were mapped to HGNC genes and only annotated ones were retained. Finally, a threshold of regulatory potential was determined to further filter some interactions based on an optimization model by fitting it to the collected cell line perturbation data. Consequently, RecTFDB was constructed, consisting of 17,450 non-redundant receptor-transcription factor interactions (751 receptors and 525 transcription factors). LigRecDB and TFTGDB were updated accordingly based on layer-shared receptors and transcription factors, we finally obtained 3659 non-redundant ligand-receptor interactions (920 ligands and 751 receptors) and 373501 non-redundant transcription factor-target gene interactions (525 transcription factors and 23021 target genes), respectively.

The details of receptor-TF links inference are described below (**Text S2**).

Text S2. Inference and optimization of Receptor-TF regulatory matrix

Weighted directed graph-based random walk algorithm

To predict receptor-transcription factor pairing, we constructed a directed weighted graph $G(V, E_V)$ based on the available data sources of signaling pathways. $V = \{v_1, \cdots, v_n\}$ is the set of the interacting molecules, and E_V is the set of the observed interactions between the upstream molecule v_i and the downstream molecule v_j. An adjacent matrix W was also constructed with weight w_{ij} defined as the occurrence number of the interaction $(v_i \rightarrow v_j)$ recorded in the databases.

The link probability between receptor and transcription factor can be considered as a link prediction problem in a graph. We used the random walk with restart (RWR) algorithm (Brin and Page 1998a; Brin and Page 1998b; H. et al. 2006; Tong et al. 2006) to calculate the probability of link generation between each pair of nodes that are not directly connected. The formula for the RWR is as follows:

$$p_{t+1}^T = (1-r)Mp_t^T + rp_0^T,$$

where p_0 is initial probability vector for nodes. Given a set of source/seed nodes $S \subset V$, the value of p_0 is 1 for the seed nodes (i.e., $\frac{1}{|S|}$) and 0 for other nodes, respectively. p_t and p_{t+1} are probability vectors of nodes at time t and $t+1$, respectively. The i-th element of p_t represents the probability of the walker being at node v_i. M represents transition probability matrix, describing the random walk probability for each pair of nodes, defined as $M_{ij} = \frac{w_{ij}}{\sum_j w_{ij}}$. $r \in (0,1)$ is a restart-probability representing the probability of a walker going back to the source nodes. When the above iteration converges, p_t could approximately represent the closeness or importance score with respect to the node of interest.

The main idea of RWR algorithm is that a random particle that starts from the seed node x can transmits to its neighbor with probability $1-r$ or return to the seed node x with probability r. After several iterations, the probability of the particle staying at any other node tends to be stable and is related to the seed node initially selected. We assume that the seed node is the receptor, and when it reaches the stable state after RWR process, we can get the probability of the receptor linking with any other node (some are TF nodes). This probability was used to represent the potential regulatory ability of the receptor on the downstream gene in the protein interaction graph constructed based on prior knowledge.

Determination of restart-probability r

For the above graph $G(V, E_V)$, E_U represents the set of all possible links between each pair of nodes in V. E_N denotes a set of unobserved links that exist in E_U but not in E_V. E_M stands for missing links (such as receptor-transcription factor pairing) that cannot be detected due to incomplete collection or limitation of current technology. The task of link prediction is to find out the missing links for short.

We used 3-fold cross-validation and random sub-sampling validation (Lü and Zhou 2011) to determine the restart-probability r and to test the algorithm's accuracy. The set of observed links E_V was divided into three subsets. Each time two subsets were used as training set E_T,

and the remaining one was used as validation set E_P. Then we repeated the process 3 times, with each of the 3 subsets used exactly once as the validation set. We performed the RWR process on the graph G' constructed from the training set E_T and the RWR index would give a score of missing links E'_M in G'. In this time, the set E'_M of missing links should include the observed links in validation set E_P as they were not used to training. In principle, the score of link in E_P should be higher than that of link in E'_M but not in E_P.

The average values of AUC and Precision (Lü and Zhou 2011) in 3-fold cross-validation were taken as evaluation indexes. For the *i*-th comparison in N independent comparisons, we randomly selected two links from the set of missing links E'_M (one of two should in the validation set, denoted as l_i and the other should not existed in the validation set, denoted as l_j). If the score S_i of link l_i is higher than the score S_j of link l_j, the prediction is considered to be unsatisfactory; If the score S_i of link l_i is lower than the score S_j of link l_j, the prediction effect is considered to be satisfactory; If the score S_i is equal to the score S_j, the prediction is random. Therefore, the AUC value was calculated as follows:

$$\mathrm{AUC} = \frac{1}{N}\sum_{i=1}^{N} x_i\ ,\ \ x_i = \begin{cases} 1, & S_i > S_j; \\ 0.5, & S_i = S_j; \\ 0, & S_i < S_j. \end{cases}$$

where N is the number of independent comparisons, x_i is the prediction effect of i-th comparison.

The evaluation metric Precision measures whether the top-L links order by the RWR score in set E'_M is predicted accurately. In general, the links in E_P should rank higher than the links in E'_M but not in E_P. Precision is defined as the frequency of links in E_P in L=100 random selection of ordered links:

$$\mathrm{Precision} = \frac{1}{L}\sum_{i=1}^{L} x_i\ ,\ \ x_i = \begin{cases} 1, & l_i \in E_P; \\ 0, & l_i \notin E_P. \end{cases}$$

Where L is the number of random selections, l_i represents the selected link in the i-th selection. Finally, considering both AUC and Precision, the optimal value of r is determined to be 0.61 (**Fig S31B**). After determining parameter in the RWR process, we could obtain the potential regulatory ability of the receptor on the downstream gene (TF).

Determination of threshold for receptor-TF regulatory matrix based on cell line data

We observed that in the regulatory potential matrix, most of the upstream receptors' regulatory potential to the downstream transcription factors is not zero. This is owing to that the receptor nodes can reach any protein nodes in the directed weighted graph via random walks except isolated nodes and nodes with zero in-degree. We therefore select a quantile cutoff θ (quantile.cutoff) to retain significant receptor-transcription factor interactions based on gene expression data of cell line perturbation experiments. 129 sets of cell line perturbation data (**Table S3**) were collected and analyzed to explore the regulation of upstream signal molecules (ligand, receptor) to downstream target genes via ligand treatment or receptor interference in a single cell line.

Firstly, three matrices were constructed according to the prior database: Ligand-receptor

regulatory matrix A, receptor-transcription factor regulatory potential matrix B and transcription factor-target gene regulatory matrix C. Denote $a_{i,j}, c_{k,t}$ and $b_{j,k}$ to represent the number of pairing occurrences in the prior database (ligand-receptor pairing, transcription factor-target gene pairing) and the regulatory potential (receptor-transcription factor pairing), with i, j, k, t indicating the index of ligand, receptor, transcription factor and target gene, respectively. For regulatory potential matrix B, we set the quantile cutoff θ to redefine $b_{j,k}$,:

$$b_{j,k} = \begin{cases} b_{j,k}, & b_{j,k} \geq b_\theta \\ 0, & b_{j,k} < b_\theta \end{cases}, \quad \theta \in (0,1)$$

where b_θ is θ-quantile threshold for the regulatory potential matrix B.

On the other hand, we analyzed differentially expressed genes (DEGs) using limma (padj<=0.05, |logfc| >= 1) for each cell line under specific perturbations (ligand treatment or receptor knockdown/mutant). The DEGs corresponding to a specific ligand or receptor was regarded as potential target genes regulated by a specific ligand (L_l) or receptor (R_r). Consequently, the ligand-target gene matrix $D_{l,m}$ and receptor-target gene matrix $E_{r,n}$ were defined as follows:

$$D = \begin{cases} 1, & TG_m \text{ is the DEG of } L_l \\ 0, & TG_m \text{ is not the DEG of } L_l \end{cases}$$

$$E = \begin{cases} 1, & TG_n \text{ is the DEG of } R_r \\ 0, & TG_n \text{ is not the DEG of } R_r \end{cases}$$

Define matrix ${}^1ABC = sgn(A \cdot B \cdot C)$, and let $\widetilde{F_1}$ be a submatrix of ${}^1\mathrm{ABC}$ that preserves the same column and row with D. Performing Hadamard product between $\widetilde{F_1}$ and D to get a ligand-target validation matrix $F1$ which integrates prior database information and cell line perturbation data information. Similarly, we can obtain matrix ${}^1BC$ and receptor-target gene validation matrix $F2$ based on the priori matrices, C and E.

We selected optimal threshold by solving the following optimization problem,

$$\theta^* = \arg\max_\theta abs\left(\frac{\frac{\Sigma(F_1)}{\#(F_1)}}{\frac{\Sigma(D)}{\#(D)}} + \frac{\frac{\Sigma(F_2)}{\#(F_2)}}{\frac{\Sigma(E)}{\#(E)}} - \frac{\Sigma({}^1ABC)}{\#({}^1ABC)} - \frac{\Sigma({}^1BC)}{\#({}^1BC)}\right)$$

where $\#(\cdot)$ represents the total number of elements of the matrix, and $\Sigma(\cdot)$ represents the number of the nonzero elements of the matrix. The first two terms of the objective function were used to preserve the information of DEGs in the cell line data as much as possible, and the last two terms were used to ensure the sparsity of the regulatory matrix. A series of values for θ was screened to maximize the above objective function. Finally, the optimal value of cutoff θ was determined as 0.98 (**Fig S31C**).

Text S3. Implementation of compared methods

We selected CellChatV2, COMMOT, CytoSignal, CytoTalk, NicheNet, MISTy, and Scriabin to compare the performance with stMLnet. Here we described the details of implementing these comparison methods.

CellChatV2. We followed the tutorial described on the CellChat website: https://github.com/jinworks/CellChat/blob/main/tutorial/CellChat-vignette.Rmd. We set the parameter “type” as ‘truncatedMean’ in the ‘computeCommunProb’ function.

COMMOT. We referred to the guideline provided by this website: https://commot.readthedocs.io/en/latest/notebooks/visium-mouse_brain.html to perform COMMOT. We then used the tradeSeq to identify the differential expression gene for downstream analysis, which is consistent with the original paper.

CytoSignal. We referred to the guideline provided by this website: https://github.com/welch-lab/cytosignal and followed the tutorial titled 'Infer spatially resolved cell-cell communication signaling at cellular resolution' to implement CytoSignal. Notably, CytoSignal performs LR interaction inference at single-cell resolution. For subsequent benchmark metric calculations, we aggregated the LR pair scores by computing their average at the cluster level.

CytoTalk. We followed the commands described on the CytoTalk website: https://github.com/tanlabcode/CytoTalk. We defined the parameters 'cutoff_a' and 'cutoff_b' as 0.05, indicating that only the ligands/receptors expressed by more than 5% of the sending/receiving cells were retained.

NicheNet. We followed the guideline described on the GitHub repository: https://github.com/saeyslab/nichenetr/tree/master?tab=readme-ov-file. The interaction-changed genes (i.e., ICGs) identified through the ‘findICG’ and ‘filterICG’ functions serve as target gene sets of interest to predict ligand targets between the sending and receiving cells.

MISTy. We adhered to the guidelines outlined on the MISTy website: https://github.com/saezlab/mistyR. Marker genes, comprising ICGs and receptors, were employed within the intra-view analysis, while ligands were utilized as markers in the para-view analysis. The para-view radius was set to 10.

Scriabin. We followed the instructions described on the Tangram website: https://github.com/BlishLab/scriabin/tree/main/vignettee. Notably, Scriabin inferred LR interactions at single-cell resolution. Therefore, we computed the average score of LR pairs at the cluster level for subsequent calculation of benchmark metrics.

Text S4. Dataset collection and processing

Single-cell resolution ST datasets

Several single-cell resolution ST datasets generated from different technologies, including seqFISH+, Slide-seq v2, MERFISH and Stereo-seq, were collected for demonstration the applicability of stMLnet. The seqFISH+ data of mouse cortex contains 10000 genes measured in 913 cells (Eng et al. 2019). The Slide-seq v2 data of mouse hippocampus contains 53173 cells and 13854 genes (Stickels et al. 2021). The MERFISH data is a 3D spatial expression dataset of mouse hypothalamus preoptic region, consisting of 155 genes from ~1 million single cells in 12 non-continuous tissue slices (Moffitt et al. 2018b; Moffitt et al. 2018a). The stereo-seq data was generated from sequencing developing mouse embryos at the E16.5 stage, consisting of 18 sections (Chen et al. 2022). This paper focus on the E1S3 section of the E16.5 stage for stMLnet analysis, encompassing 155741 cells with 28579 genes per cell. We annotate the data using marker genes provided in the original paper. These datasets were downloaded, preprocessed, and annotated by using Seurat and Giotto according to the procedures described in the original tutorial. The processed dataset was used as input of stMLnet. The unannotated cells were filtered. The ligand and receptor genes were selected by their mean gene expression and gene expression percentage. For the seqFISH+ dataset, Slide-seq v2 dataset, and Stereo-seq data, cell type-specific genes selected by using ‘findMarkers’ function in Seurat (Hao et al. 2021) were used as the target gene set of interest for input. For the MERFISH dataset, cell type-specific genes selected via ‘findMarkers_one_vs_all’ function in Giotto (Dries et al. 2021) were used as the target gene set of interest for input of stMLnet.

Breast cancer-1 dataset

Breast cancer ST data were obtained by performing spatially resolved transcriptomics (10x Visium technology) on 6 samples from triple negative breast cancer (Wu et al. 2021). We chose ‘CID4465’ sample for further analysis in this paper. The preprocessing of the ST data, including quality control, normalization, and dimension reduction (tSNE analysis), was conducted using standard pipeline of Seurat. We utilized a probabilistic model named Sterescope (Andersson et al. 2020) to deconvolute the cellular composition of each spot using scRNA-seq data matched with clinical subtypes. This methodology is consistent with the approach outlined in the original paper. We then adopted the 'runALRA' function in Seurat (Linderman et al. 2022) to complete the imputation of the gene expression matrix, thereby reducing the impact of gene expression sparsity on subsequent analysis. We additionally utilized the ‘findICG’ and 'filterICG' functions with default parameters in Giotto (Andersson et al. 2020; Dries et al. 2021) to acquire ICG, which was then inputted into stMLnet as a target gene set of interest.

Breast cancer-2 dataset

The 10x Visium ST data of ductal carcinoma were downloaded from 10x Genomics website (https://www.10xgenomics.com/datasets/human-breast-cancer-block-a-section-1-1-standard-1-1-0). The preprocessing of the ST data, including quality control, normalization, and dimension reduction (tSNE analysis), was conducted using standard pipeline of Seurat. The cell type annotation information in a scRNA-seq dataset (GSE118389) (Karaayvaz et al. 2018) was mapped to each spot of the ST data ('FindTransferAnchors' and 'TransferData' in

Seurat v3.2.3 (Stuart et al. 2019)), according to the previous study (Li et al. 2023). Furthermore, the cell type-specific gene expression for the dominant cell type in each spot was calculated using ‘get_decomposed_data’ function in RCTD v1.1.0 (Cable et al. 2022) with the aid of the cell type proportion matrix from Seurat output and the above scRNA-seq reference dataset. We also employed Giotto (Dries et al. 2021) to get ICGs by using 'findICG' function and 'findICG' function with default parameters, which were used as the input target gene set of interest for stMLnet. The ST data was imputed using Seurat 'runALRA' function to mitigate the sparsity of the expression matrix for the LR signaling quantification and random forest regression.

Glioma dataset

The ST data of glioma was generated by 10X Visium technology (Ravi et al. 2022). This dataset includes spatially resolved transcriptomics data of 28 samples. In this study, we selected sample ‘#UKF304_T’ for subsequent analysis. The preprocessing of the ST data, including quality control, normalization, and dimension reduction (tSNE analysis), was conducted using standard pipeline of Seurat. Following the original study (Ravi et al. 2022), the SPOTlight method was used to decompose each spot into individual cell type with the aid of scRNA-seq data (GSE84465). Furthermore, we used the Seurat 'runALRA' function to perform imputation on the expression matrix of ST data to reduce the impact of gene expression sparsity on subsequent analyses. And then, we adopted the ‘get_decomposed_data’ function in RCTD v1.1.0 to calculate the cell type-specific gene expression for the dominant cell type in each spot.

To select target genes of interest as input for stMLnet, we collected a set of RNA-seq data of the isolated glioma cells or macrophages from three groups of mice with different responses to the CSF1R inhibitor treatment (Reb, rebound; EP, endpoint; Vel, vehicle) (GSE69104 (Quail et al. 2016)). After CPM standardization, low-expression genes with expression levels below 0.5 in more than 6 samples were filtered. We calculated differentially expressed genes (DEGs) in macrophages between different groups (Reb v.s. EP, EP v.s. Veh) using limma test ($|logfc|>1$, $p.adj<0.1$). The DEGs between Reb and EP could be viewed as resistance-related genes, which were input to stMLnet as potential target genes in macrophages or tumor cells to infer their upstream regulators.

For other cell types (e.g., T cells and oligodendrocytes), we used highly expressed genes in these cell types, analyzed from the scRNA-seq data by using ‘FindMarkers’ function in Seurat ($|logfc|>2$, $p.adj<0.05$, $pct>=0.1$), as respective target genes of interest for stMLnet input.

In addition, the DEGs in macrophages between EP and Veh groups could be viewed as genes responsive to CSF1R inhibition and thus potentially regulated by CSF1R, which were used to test the prediction of stMLnet with respect to the CSF1R-regulated target genes.

COVID-19 dataset

The ST data of COVID-19-infected human lung tissue was processed with the original code deposited at Mendeley: https://doi.org/10.17632/xjtv62ncwr.1. Following the original study (Gracia Villacampa et al. 2021), the NNMF method and the Pearson correlation were used to calculate spot-factor matrix and factor-celltype matrix to calculate cell type proportion for each spot in the ST data. More specifically, we firstly merged the similar subtypes according to the reference scRNA-seq dataset (Travaglini et al. 2020) and then two truncation parameters

(factor_cutoff = 0.5 and celltype_cutoff = 0.5) related to spot-factor matrix and factor-celltype matrix were utilized to avoid excessive dispersion of cell type proportion. The cell type proportion matrix was defined as the Hadamard product of the above two matrices. The cell type with the largest proportion in each spot was assigned to each spot. The cell type-specific gene expression for the dominant cell type in each spot was calculated using 'get_decomposed_data' function in RCTD v1.1.0 (Cable et al. 2022). We then adopted the 'runALRA' function in Seurat to complete the imputation of the gene expression matrix, thereby reducing the impact of gene expression sparsity on subsequent analysis. The cell type-specific DEGs in the ST data in each type of receiver cells (analyzed using 'FindMarkers' function in Seurat) were selected as the target genes of interest for input of stMLnet to infer multilayer signaling networks.

Cell lines data

To calibrate parameters for prior information integration, we collected 15 datasets of cell line gene expression that were treated with ligands or perturbed by receptor knockout/mutation from the GEO database (**Table S5**), involving 3 tissues, 15 cell lines, 6 ligands and 4 receptors. We used limma (E et al. 2015) to select DEGs of each cell line (before vs. after perturbation) under criteria of |logfc| >1 and p.adj<0.05. Ultimately 15 datasets, each with more than 50 DEGs, were used for correction of prior databases in this study.

Text S5. Simulation study

To evaluate the quantitative model involved in stMLnet, we benchmarked stMLnet with a set of synthetic data of spatial gene expressions. We consider 5 ligands, 2 receptors, 3 TFs and 4 target genes. The ground truth of the multilayer network is shown in **Fig 3A**.

We simulate 3 types of cells, including 2 types of sender cells (SC_1 and SC_2) and 1 type of receiver cells (RC). These cells are randomly located at a fraction of grids within a 2-dimensional lattice (100×100) that simulates a square domain of tissue slice ($\Omega \subset \boldsymbol{R}^2$). The ligand genes are expressed by the sender cells and the products are subject to diffusion. The receptor genes, TFs and TGs of the receiver cells do not diffuse across microenvironment.

The spatial-temporal changes of the extracellular ligands are modeled using the following reaction-diffusion equation

$$\frac{\partial[L_i]}{\partial t} = D_i \Delta[L_i] + \sum_k r_{ik}\chi_{SC_k}(x) - d_i[L_i] \tag{S1}$$

where $[L_i] = [L_i](x,t)$ represents the concentration of the ligand L_i at location $x \in \Omega$ and time t. D_i and d_i represents, respectively, the diffusion coefficient and degradation rate of the ligand L_i. r_{ik} is the release rate of the ligand L_i by sender cells SC_k $(k = 1 \text{ or } 2)$. $\chi_{SC_k}(x)$ is an indicator function of the sender cells, taking value 1 where there is a sender cell at location x, and 0 otherwise. Random initial value and the no-flux boundary condition are imposed to the above equation.

The level of each receptor is assumed steady through the simulation. The activation of each TF within the receiver cells is modulated by the upstream LR signaling, which is described as follows,

$$\frac{d[TF_l]}{dt} = \sum_j \alpha_{jl} \sum_i b_{ij}[L_i] \cdot [R_j] - \beta_l[TF_l] \tag{S2}$$

where $[TF_l] = [TF_l](x,t)$ represents the activation level of the TF_l at location x and time t. b_{ij} equals to 1 or 0, representing binding or non-binding between ligand L_i and receptor R_j. α_{jl} is the activation coefficient of TF_l by R_j. β_l is the degradation rate of TF_l.

The expression of each target gene is regulated by TFs, which is described as follows,

$$\frac{d[TG_s]}{dt} = \sum_l \mu_{ls}[TF_l] - \gamma_s[TG_s] \tag{S3}$$

where $[TG_s] = [TG_s](x,t)$ represents the expression level of the target gene TG_s at location x and time t. μ_{ls} is the regulatory coefficient of TG_s expression by TF_l. γ_s is the degradation rate of TG_s.

To get the steady-state values of spatial gene expression, we solve the following equations:

$$\begin{aligned} -D_i\Delta[L_i] &= \sum_k r_{ik}\chi_{SC_k}(x) - d_i[L_i] \\ \left.\frac{\partial[L_i]}{\partial \vec{n}}\right|_{\partial\Omega} &= 0 \end{aligned} \tag{S4}$$

$$[TF_l](x) = \frac{1}{\beta_l}\sum_j \alpha_{jl}\sum_i b_{ij}[L_i]\cdot[R_j] \tag{S5}$$

$$[TG_s](x) = \frac{1}{\gamma_s}\sum_l \mu_{ls}\,[TF_l] \tag{S6}$$

Equations (S4) were solved using finite difference method with five-point central difference scheme (see details below). The values of some parameters (e.g., r_{ik}, α_{jl}, β_l, μ_{ls}, γ_s and $[R_j]$) in the above model were randomly sampled in each simulation. By simulating the above model with random parameter values 100 times, we got 100 sets of synthetic data each includes spatial expression values of 5 ligands, 2 receptors and 4 target genes and location coordinates of the SCs and RCs. **Fig S3** illustrate a set of representative simulation data. Such spatial expression data was used as input of the random forest regression model in stMLnet (without using the prior information of the predefined multilayer network) to infer the regulation of TGs' expression by LR pairs. The predicted importance scores for LR-TG regulations were benchmarked with the ground truth.

To numerically solve Equation (S4), we employed finite difference method with five-point central difference scheme. For simplicity, we wrote the Equation (S4) into the following form by ignoring index i:

$$\begin{cases} -D\Delta u(x,y) = \sum_k r_k \chi_{SC_k}(x,y) - d\cdot u(x,y), \quad (x,y)\in\Omega \\ \dfrac{\partial u(x,y)}{\partial \vec{n}} = 0, \quad (x,y)\in\partial\Omega = \Gamma \end{cases}, \tag{S7}$$

where $\Omega = \{(x,y)\,|\,a_1 \le x \le b_1,\ a_2 \le y \le b_2\}$. We first uniformly divided the whole domain into $\bigcup_{i=0}^{m}\bigcup_{j=0}^{n}[x_i, x_{i+1}]\times[y_i, y_{i+1}]$, here $x_i = a_1 + i\cdot h_1$, $h_1 = (b_1 - a_1)/m$, $i = 0,1,\cdots,m$, and $y_j = a_2 + j\cdot h_2$, $h_2 = (b_2 - a_2)/n$, $j = 0,1,\cdots,n$.

Assume that (x_i, y_j) is a regular interior point. Denote $u_{ij} = u(x_i, y_j)$, $f_{ij} = \sum_k r_k \chi_{SC_k}(x_i, y_j)$. By using five-point central difference stencils to approximate the diffusion term, we get

$$u_{xx} \approx \frac{u_{i-1,j} - 2u_{ij} + u_{i+1,j}}{h_1^2},$$

$$u_{yy} \approx \frac{u_{i,j-1} - 2u_{ij} + u_{i,j+1}}{h_2^2}.$$

Therefore, at each interior point (x_i, y_j), we get the following difference equations

$$-D\left(\frac{u_{i-1,j} - 2u_{ij} + u_{i+1,j}}{h_1^2} + \frac{u_{i,j-1} - 2u_{ij} + u_{i,j+1}}{h_2^2}\right) = f_{ij} - du_{ij}, \tag{S8}$$

$$i = 1, \cdots, m-1, \quad j = 1, \cdots, n-1.$$

Order the $\{u_{ij}\}$ and $\{f_{ij}\}$ into a 1-dimensional vector as follows

$$\boldsymbol{u} = \left(u_{11}, u_{21}, \cdots, u_{m-1,1}, u_{21}, \cdots, u_{m-1,2}, \ldots, u_{1,n-1}, \cdots, u_{m-1,n-1}\right)^T,$$

$$\boldsymbol{f} = \left(f_{11}, f_{21}, \cdots, f_{m-1,1}, f_{21}, \cdots, f_{m-1,2}, \ldots, f_{1,n-1}, \cdots, f_{m-1,n-1}\right)^T.$$

At the boundary points, by discretizing the boundary conditions, we have

$$u_{0,:} = u_{1,:};\ u_{m,:} = u_{m-1,:};\ u_{:,0} = u_{:,1};\ u_{:,n} = u_{:,n-1}.$$

These constrains could be incorporated into the Equations (S8).

We next sought to represent the above Equations (S8) with matrix form.

Denote

$$\boldsymbol{d}_{xx} = -Dh_1^2 \begin{bmatrix} -2 & 2 & & \\ 1 & -2 & 1 & \\ \ddots & \ddots & \ddots & \\ & 1 & -2 & 1 \\ & & 2 & -2 \end{bmatrix}_{(m-1)\times(m-1)},$$

and

$$\boldsymbol{d}_{yy} = -Dh_2^2 \begin{bmatrix} -2 & 2 & & \\ 1 & -2 & 1 & \\ \ddots & \ddots & \ddots & \\ & 1 & -2 & 1 \\ & & 2 & -2 \end{bmatrix}_{(n-1)\times(n-1)}.$$

Then the discretization matrix of $-(u_{xx} + u_{yy})$ could be represented as

$$A = I_{n-1} \otimes d_{xx} + d_{yy} \otimes I_{m-1},$$

where $\otimes$ stands for the Kronecker product, and I_{n-1} for an identity matrix of order $n-1$.

As such, the Equation (S8) could be written into the following matrix form

$$A\boldsymbol{u} = \boldsymbol{f} - d\boldsymbol{u}, \tag{S9}$$

Consequently,

$$\left(\boldsymbol{A} + d \cdot I_{(m-1)(n-1)}\right)\boldsymbol{u} = \boldsymbol{f}. \tag{S10}$$

Now the numerical solutions to the above linear algebraic equations (i.e., Equation (S10)) are readily solvable. In our simulation, we set $a_1 = a_2 = 0$, $b_1 = b_2 = 100$, and $m = n = 100$.

Text S6. Application of stMLnet on Slide-seq v2 data of mouse hippocampus

We also employed stMLnet to investigate a layer-scale spatial transcriptomic data, the Slide-seq v2 data of mouse hippocampus, which measured the expression of 23264 genes in 53173 beads (Stickels et al. 2021). Moreover, the Slide-seq v2 data contains 17 cell types, including Astrocyte (Astro), CA1-Principal (CA1-Pri), CA3-Principal (CA3-Pri), Dentate-hilum (Denta-hil), Dentate-Principal (Denta-Pri), Endothelial-stalk (Endot-sta), Endothelial-tip (Endot-tip), Entorhinal-cortex (Endot-cor), Ependymal (Epend), Interneuron (Inter), Microglia (Micro), Neurogenesis (Neuro), Oligodendrocyte (Oligo), Polydendrocyte-1 (Polyd-1), Polydendrocyte-2 (Polyd-2), Resident-macrophage (Resid-mac) (**Fig S15A**). As shown in **Fig S15B**, LR signal analysis reveals that stMLnet identified active intercellular signaling between Extor-cor and CA1-pri, consistent with the two classic pathways connecting the entorhinal cortex and hippocampus (Andersen et al. 2006; van Strien et al. 2009) Extor-cor also have active signal transmission with Inter, as previously reported (Li et al. 2017). Furthermore, **Fig S15C** demonstrates that the interaction from Extor-cor to Inter and CA1-pri is significant. Specifically, setting the Extor-cor as the sender cells, stMLnet revealed that the upstream LR signaling *Calm1-Kcnq3* and *Calm1-Ptpra* have the most prominent regulatory potential on the downstream target genes such as *Aldoc* in CA1-Pri and target gene *Sst* in Inter, respectively (**Fig S15D**, **Fig S16**). Furthermore, the multilayer signaling network (**Fig 15E-F**) more clearly delineates the multilayer regulatory pathway of L-R-TF-TG from Extor-cor to Inter and CA1-Pri.

Text S7. Robustness and scalability evaluation of stMLnet

We assessed the robustness of three hyperparameters in stMLnet's process in constructing multilayer networks: min.pct, logfc, and min.expr. The min.pct parameter indicates the minimum percentage of cells in which a gene is detected, while logfc measures the differential expression of genes across different cell populations. Meanwhile, min.expr reflects the minimum average expression level of genes across different cell populations. Among these hyperparameters, min.pct and logfc are pivotal for identifying candidate target genes using the 'FindMarker' function (from Seurat (Hao et al. 2021)) or the 'FindICG' function (from Giotto (Dries et al. 2021)), while min.pct and min.expr are critical for selecting candidate ligands and receptors based on the average expression levels of genes. Hence, we evaluated the robustness of stMLnet by applying it to infer the multilayer networks on the abovementioned Slide-seq v2 data with varying parameter settings for min.pct, min.expr, and logfc. Subsequently, we measured the consistency of stMLnet performance by computing the Jaccard coefficients between the multilayer networks inferred under different parameter settings.

The Venn diagrams in **Fig S17A-C** indicate the overlaps of subnetworks (i.e., Lig-Rec, Rec-TF, or TF-TG) under different values of the three parameters min.pct, min.expr and logfc, respectively. The values of min.pct and min.expr range from 0.00 to 0.05 with an interval of 0.01, and the range of logfc values spans from 0.00 to 0.20 with interval of 0.05. For the parameters min.pct and min.expr, we observed significant overlap in the results inferred by stMLnet for each subnetwork across various parameter settings (**Fig S17A-B**). Regarding the parameter logfc, we found that Lig-Rec and Rec-TF subnetworks predicted by stMLnet have a large portion of intersections under different logfc settings, while the overlap in TF-TG subnetworks predicted by stMLnet under varying logfc settings is relatively lower (**Fig S17C**). Additionally, the Jaccard coefficient was calculated to quantitatively evaluate the robustness of stMLnet (**Fig S17D**). We observed that the median Jaccard coefficients for the three subnetworks associated with the parameter min.pct exceed 0.5, while those for the three subnetworks linked to the parameter min.expr surpass 0.6. Specially, the median Jaccard coefficients of Lig-Rec and Rec-TF corresponding to the parameter logfc are around 0.5, while the median Jaccard coefficient of TF-TG is lower than 0.25. This difference could be attributed to the fact that the parameter setting of logfc directly determines the selection of the target gene set when applying stMLnet. Overall, stMLnet is relatively robust to the parameters min.pct and min.expr while being sensitive to the parameter logfc.

To further investigate the impact of logfc, we employed stMLnet to infer multilayer networks corresponding to varying logfc values on three different ST datasets (**Fig S18**), where the values of min.pct and min.expr were fixed on each dataset. The values of logfc ranged from 0.00 to 0.60 with an interval of 0.05. Our analysis revealed that for Slide-seq v2 and seqFISH+ datasets, as the logfc value increased, the number of target genes in the multilayer network decreases rapidly, while other types of nodes (ligands, receptors, and TFs) remain relatively stable. Accordingly, the number of links in the TF-TG subnetwork in the multilayer network exhibited a significant downward trend, while the number of links in the Lig-Rec and Rec-TF subnetworks remains basically unchanged (**Fig S18A-D**). These results indicate that the Slide-seq v2 and seqFISH+ datasets are sensitive to changes in the logfc threshold, which can affect the selection of target genes and, in turn, the multilayer network structure. For the MERFISH

data, the number of nodes (ligands, receptors, TFs, and TGs) and the number of subnetwork links in the multilayer network are completely unaffected by changes in the logfc threshold and remain stable (**Fig S18E-F**). This may be related to the limited number of genes measured in the MERFISH data, which may limit the response range of the network with respect to the varied logfc threshold. These results imply important guidance of parameter selections for the users to use stMLnet.

Furthermore, we assessed the scalability of stMLnet on large-scale ST datasets. We employed a Stereo-seq data of the E16.5 mouse embryo section (Chen et al. 2022), which contains 155741 cells and 28579 genes (**Fig S17E**). We tested the scalability of stMLnet using a down-sampling approach. We generated five datasets with different down-sampling rates (i.e., 0.1, 0.3, 0.5, 0.75, and 1) and recorded the running time and memory usage of stMLnet on these datasets. The result shows that the running time and memory usage of stMLnet increase almost linearly with the number of cells (**Fig S17F, Fig S19**), suggesting good scalability of stMLnet on large-scale ST datasets. In addition, we used these five datasets to evaluate the robustness of stMLnet to variations in cell type abundances (**Fig S20A**). We evaluated the overlap between subnetworks inferred by stMLnet on these five datasets. The median Jaccard coefficients of the three subnetworks were all above 0.75 (**Fig S20B**), indicating significant overlap among the subnetworks inferred by stMLnet under different cell type abundances. Additionally, the Venn diagrams (**Fig S20C**) further verify the robustness of stMLnet with respect to cell type abundance.

Finally, we evaluated the robustness of stMLnet with respect to gene dropout using the MERFISH dataset. Using the section 6 slice of the MERFISH dataset, we sequentially dropped out 161 genes, one at a time, and used stMLnet to infer the corresponding multilayer networks. We then calculated their overlap rate with the original multilayer network (without dropout) to quantify the impact of gene dropout (**Fig S21**). An overlap rate of 100% indicates that the subnetwork remains identical to the original even after a specific gene is dropped out. For the Lig-Rec subnetwork, we found that 83.85% (135/161) of the genes were completely consistent with the original network after dropout (i.e., overlap rate = 100%) (**Fig S21A**). This indicates that the dropout of most genes had little effect on the structure of the Lig-Rec subnetwork, highlighting its strong robustness to changes in individual genes. For the Rec-TF subnetwork, the dropout of 146 genes (90.68%) led to a subnetwork overlap rate higher than 85%, of which 84 genes (52.17%) had an overlap rate of 100%, that is, the Rec-TF subnetwork after dropout was exactly the same as the Rec-TF subnetwork without dropout (**Fig S21B**). Compared with the Lig-Rec subnetwork, the Rec-TF subnetwork is more sensitive to gene dropout, but still shows high robustness. For the TF-TG subnetwork, 80 genes (49.69%) had an overlap rate of 100%, which indicates that the TF-TG subnetwork is more sensitive to gene dropout than the Lig-Rec and Rec-TF subnetworks (**Fig S21C**). In summary, within the multilayer network constructed from the MERFISH dataset, the Lig-Rec subnetwork exhibits higher robustness to gene dropout compared to the Rec-TF and TF-TG subnetworks. This suggests that the inference of intercellular LR interactions by stMLnet is more reliable than the intracellular regulation predictions on FISH-based ST datasets.

Text S8. Comparison of prior databases

We here discuss the difference of the prior databases in stMLnet and those in other tools such as NicheNet and Omnipath. stMLnet collected not only intercellular communication interactions (ligand-receptor interactions), but also intracellular signaling interactions (receptor-transcription factors, transcription factor-target gene interactions). At present, NicheNet collected interactions from 57 resources, while Omnipath collected interactions from more than 100 resources. The main differences between them and stMLnet are as follows.

(1) *Data collection resources and standards*. (i) At the ligand-receptor interaction level, stMLnet included information from NicheNet and Omnipath at the ligand-receptor interaction level, so its ligand-receptor pairs largely overlap with NicheNet and Omnipath (**Fig S31A**, left panel). (ii) At the level of intracellular signaling interactions, NicheNet collected not only a large amount of protein interaction information but also a lot of self-annotated interaction information. As such, signaling pairs in NicheNet were far more than those of stMLnet and Omnipath (**Fig S31A**, middle panel). (iii) At the transcriptional regulation level, stMLnet collected many TF-TG interactions for better leveraging the expression data of cell line perturbation experiments to determine significant signaling path from specific receptors to TFs (**Text S2**). Therefore, stMLnet has much more information on regulatory interactions than NicheNet and Omnipath (**Fig S31A**, right panel).

(2) *Prediction of directed interactions*. stMLnet selected receptor-transcription factor interactions with highly regulatory potential by collecting information mainly from pathway databases (PathBank, SMPDB, Reactome, KEGG, BioCarta, NCI, PATHER, PharmGKB) (**Fig S31C**). While NichNet and Omnipath mainly collected such information from protein-protein interaction databases besides signaling pathway databases. We know that receptor-TF signal transduction has obvious direction. While the information collected from pathway database generally has obvious signal transmission direction (ligand-receptor-downstream signal molecule-transcription factor-target gene), but there are a lot of molecular interactions with unknown directions in protein-protein interaction databases. Therefore, bias may be introduced by using protein-protein interaction database information when constructing a directed graph to predict receptor-transcriptional factor interactions. Therefore, NicheNet and Omnipath, although collecting more abundant data resources, were not as effective as stMLnet in predicting directed interactions (**Fig S31B**).

Text S9. Inference of multilayer signaling networks

To predict significant multilayer signaling networks, we first identify specific ligand genes, receptor genes, and feature genes from the input data. Next, stMLnet utilizes LigRecDB to search for the paired links between the identified ligands and receptors, constructing a Lig-Rec subnetwork. Feature genes are then intersected with the TG nodes in TFTGDB and linked to their corresponding TFs to form a TF-TG subnetwork. Subsequently, the TF nodes in the TF-TG subnetwork are matched with RecTFDB to construct the Rec-TF subnetwork. The Lig-Rec subnetwork is further updated by incorporating receptor nodes involved in the Rec-TF subnetwork. Additionally, Fisher's exact test can be applied to further refine the network by filtering out inactive TFs, receptors, and their associated interactions. Finally, the individual subnetworks are integrated to construct a comprehensive multilayer signaling network (**Fig. 1C**). Below we describe the details of the multilayer network structure inference.

Constructing ligand-receptor subnetwork

Based on the LigRecDB, we selected highly expressed ligands and receptors as potential ligand and receptor genes. Genes with an average expression level above a predefined threshold (e.g., min.expr = 0.05 by default) and expressed in more than a specified percentage of cells (e.g., 10% of cells by default) in sending cells were categorized as highly expressed ligands (LIGs). Similarly, the highly-expressed genes in the receiver cells with average expression level greater than a threshold (e.g., min.expr = 0.05 by default) and expression percentage more than a threshold (e.g., 10% cells by default) constituted the set of highly-expressed receptors (REGs). These LIGs and REGs were then screened in LigRecDB to construct the ligand-receptor subnetwork, denoted as $N_{LIG-REC}$. We provide the above pipeline as the default procedure in stMLnet to select potential ligands and receptors. Additionally, stMLnet allows users to input gene sets of interest that are selected by other methods as candidate ligand and receptor sets.

Constructing TF-target gene subnetwork

Users can input a set of predefined genes associated with a phenotype or biological function of receiver cells to infer their upstream signaling pathways involving TFs and LRs, orchestrated by cell-cell interactions. In this study, we refer these input genes as "feature genes", which can be set as differentially expressed genes (DEGs) (via, e.g., 'FindMarkers' function in Seurat (Dries et al. 2021; Hao et al. 2021)) or interaction-changed genes (ICGs) (via, e.g., 'findICG' function in Giotto (Dries et al. 2021)), or input by users according to their purpose. The set of input feature genes is denoted as FGs, other genes were denoted as $nFGs$. We used Fisher's exact test to calculate a p-value for each TF_i as follows:

$$p_i = \binom{a+b}{a}\binom{c+d}{c}/\binom{a+b+c+d}{a+c}, \quad \text{(S11)}$$

where $\binom{m}{n}$ represents the binomial coefficient. We denoted TGs as the genes regulated by TF_i and $nTGs$ as the genes not regulated by TF_i. $a = |FGs \cap TGs|$ represents the number of genes in the intersection between input feature genes and TF_i-regulated target genes. $b = |FGs| - a$ represents the number of genes that are in the input feature gene set but are not regulated by TF_i. $c = |TGs| - a$ represents the number of genes that are regulated by TF_i but

are not belong to the input feature gene set. $d = |FGs \cap nTGs|$ represents the number of genes that are neither in the input feature gene set nor regulated by TF_i. If the Fisher's exact p-value $p_i \leq 0.05$, then the TF_i is considered to be significantly activated. All the activated TFs constitute a set $aTFs$. As a result, we get the TF-target gene subnetwork N_{TF-TG} by paring TFs in $aTFs$ with genes in FGs.

Constructing receptor-TF subnetwork

The construction of receptor-TF subnetwork is similar to that of TF-target gene subnetwork. We employed Fisher's exact test to calculate a p-value for each receptor REC_i as follows:

$$p'_i = \binom{a'+b'}{a'}\binom{c'+d'}{c'}\Big/\binom{a'+b'+c'+d'}{a'+c'}, \quad \text{(S12)}$$

We denoted TFs to represent the TFs regulated by REC_i and $nTFs$ the genes that are not regulated by REC_i. $a' = |aTFs \cap TFs|$ represents the number of TFs in the intersection set between the activated TFs and REC_i-regulated TFs. $b' = |aTFs| - a'$ represents the number of TFs that are activated but are not regulated by REC_i. $c' = |TFs| - a'$ represents the number of TFs that are regulated by TF_i but are not activated. $d = |naTFs \cap nTFs|$ represents the number of TFs that are neither activated nor regulated by REC_i. If the Fisher's exact p-value $p'_i \leq 0.05$, then the REC_i is considered to be significantly activated. All the activated receptors constitute a set $aRECs$. As a result, we get the receptor-TF subnetwork N_{REC-TF} by paring receptors in $aRECs$ with TFs in $aTFs$ based on the RecTFDB database.

When the number of genes in ST data (e.g., MERFISH data) is limited, the application of Fisher's exact test may result in too few TF-TG pairs in the subnetwork N_{TF-TG} as well as too few receptor-TF links in the subnetwork N_{REC-TF}. This can lead to the exclusion of key signaling molecules. In such cases, we can directly pair genes in FGs with their corresponding TFs based on the TFTGDB database to construct the gene subnetwork N_{TF-TG}. We then directly pair TFs in the subnetwork N_{TF-TG} with their corresponding receptors using the RecTFDB database to construct the subnetwork N_{REC-TF}.

Integrating subnetworks into a multilayer network

The above subnetworks were connected together into a multilayer signaling network $N_{L-R-TF-TG}$ by pruning the nodes and links that are not the downstream of the activated LR signaling or activated TFs. Through the above steps, the constructed multilayer signaling network contains different numbers of Lig-Rec pairs, Rec-TF links, and TF-TG pairs for different input feature gene sets.

Text S10. Importance score of ligand/receptor-target regulations

Based on the random forest model, we could calculate the importance score of the k_t-th feature (LRS^{k_t}) contributing to the expression of target gene TG_t, and thereby rank LR pairs. Moreover, we also refined the permutation importance score to account for the disassembled importance of L or R alone, which was referred to as partial importance score.

Importance score of LR pairs

We calculated permutation-based feature importance for each LR pair by evaluating mean-squared-error (MSE) between the random forest (RF) model prediction and the true values on out-of-bag (OOB) samples and comparing the change of the MSE before and after the permutation of the LR activities. If the MSE is largely increased after LR permutation, then the LR pair is viewed to be important with respect to regulating the target gene expression. To integrate the computed importance scores for the m target genes and avoid the bias originated from the variance in gene expression, we normalized the input and the output (*Z*-score) of the random forest regression model before running it (Huynh-Thu et al. 2010). Consequently, the importance scores computed from the TG_t model were denoted as

$$IM_t = \left(im_{1_t}, im_{2_t}, \dots, im_{n_t}\right),\ t = 1, 2, \dots, m\,. \tag{S13}$$

where im_{k_t} represents the importance score of the k_t-th LR pair for the TG_t expression. Integrating the importance scores computed from the m models, we get

$$IM = \left(im_{1_1}, \dots, im_{n_1}, \dots, im_{1_m}, \dots, im_{n_m}\right). \tag{S14}$$

As such, we could compare the importance scores of LR pairs across different regression models.

Partial importance score of L or R

The above importance score was defined for the combination of the ligand and the receptor. To decompose the importance score for the ligand or receptor alone in each LR pair, we modified the above permutation-based feature importance method to account for the partial importance score (PIM) of the upstream regulator molecules (ligand or receptor, denoted as $V_q,\ q = 1_t, 2_t, \dots, q_t$) for the target gene TG_t. Specifically, the PIM was computed as follows:

1) For each regression tree, compute the MSE using the OOB data, denoted as $errOOB_1$;

2) Randomly permute the values of the features (LR pairs) involving V_q on all the OOB samples and then compute the MSE using the OOB data, denoted as $errOOB_2$;

3) For the random forest with N trees, the PIM of the upstream regulator molecule V_q could be calculated as

$$pim_{q_t} = \frac{\sum(errOOB_2 - errOOB_1)}{N}, \tag{S15}$$

Ultimately, the partial importance scores of the upstream regulators computed from the random forest model f_t were

$$PIM_t = \left(pim_{1_t}, pim_{2_t}, \dots, pim_{q_t}\right), \tag{S16}$$

According to the ranking in the above PIM_t, we could compare the regulatory capabilities of different upstream regulatory molecules for the target gene TG_t. On the other hand, integrating the partial importance scores computed from the m models, we get

$$PIM = \left(pim_{1_1}, \ldots, pim_{q_1}, \ldots, pim_{1_t}, \ldots, pim_{q_t}, \ldots, pim_{1_m}, \ldots, pim_{q_m}\right). \quad \text{(S17)}$$

This enables us to compare the regulatory capabilities of a given upstream regulators with respect to different target genes.

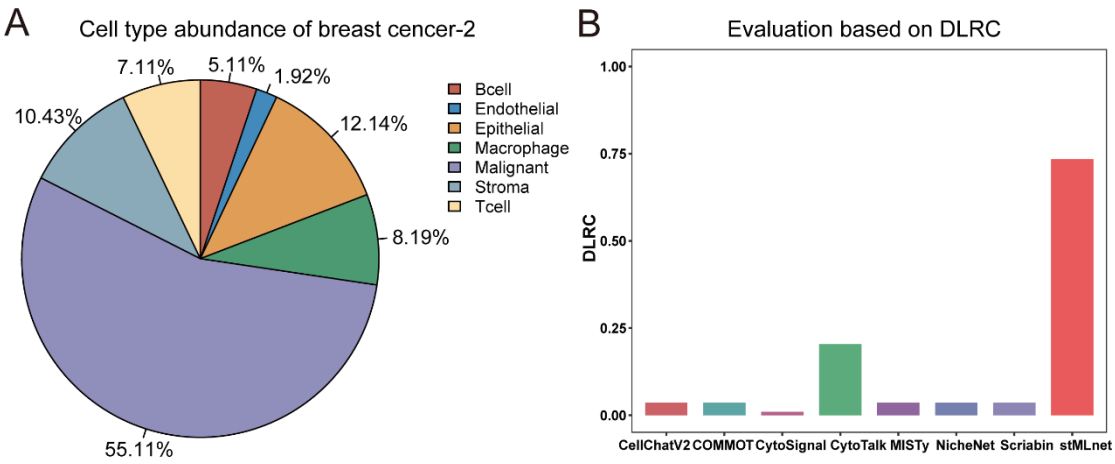

Figure S1. Evaluation of the performance of stMLnet for inferring intercellular communication between rare cell types on breast cancer-2 dataset. (A) Pie plot of the percentage of each cell type on breast cancer-2 dataset. Each color represents an individual cell type, and the number next to each sector represents the percentage of cells of a cell type to the total number of cells. (B) Bar plot of DRLC values of eight LR inference methods, including CellChatV2, COMMOT, CytoSignal, CytoTalk, MISTy, NicheNet, Scriabin, and stMLnet, on the communication between Endothelial cells and other cell types.

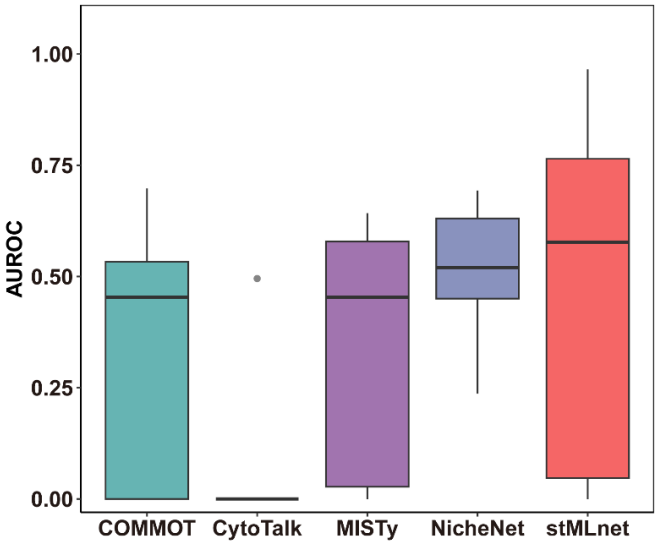

Figure S2. Evaluation and comparison of the 5 L/R-TG inference methods using the AUROC metric. Box plot of AUROC values of L/R-Targets inference methods, including COMMOT, CytoTalk, MISTy, NicheNet, and stMLnet, across three ST datasets. The L/R-Targets scores inferred by these methods were compared to the differential expression states of targets (DEGs) in the cell line datasets.

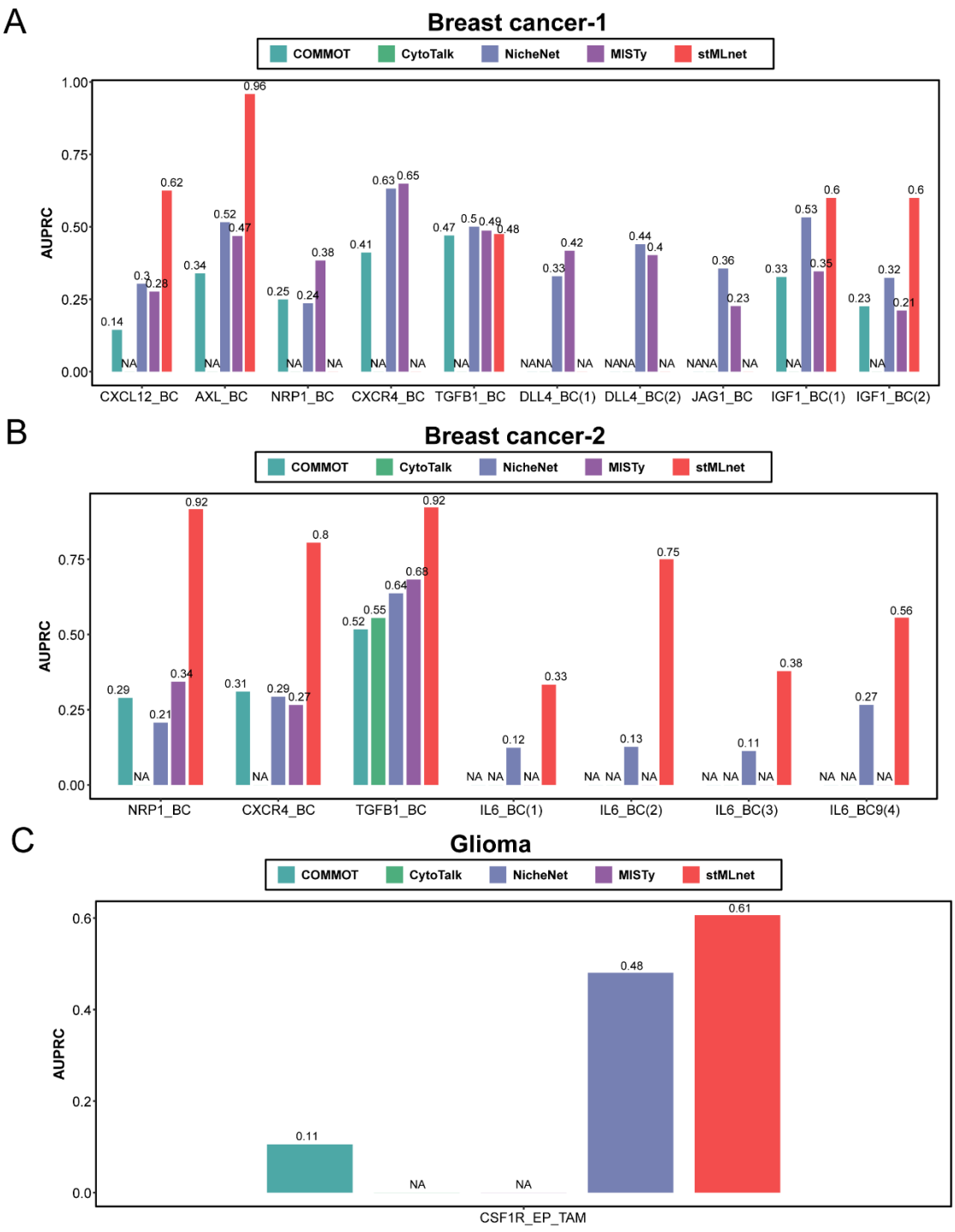

Figure S3. Bar plot of AUPRC values of L/R-Target predicted from different ST datasets and validated by different perturbation-expression datasets. (A), (B), and (C) represent the AUPRC results of Breast cancer-1, Breast cancer-2, and Glioma as the input ST datasets. 'NA' indicates that the method falls failure in AUPRC calculations.

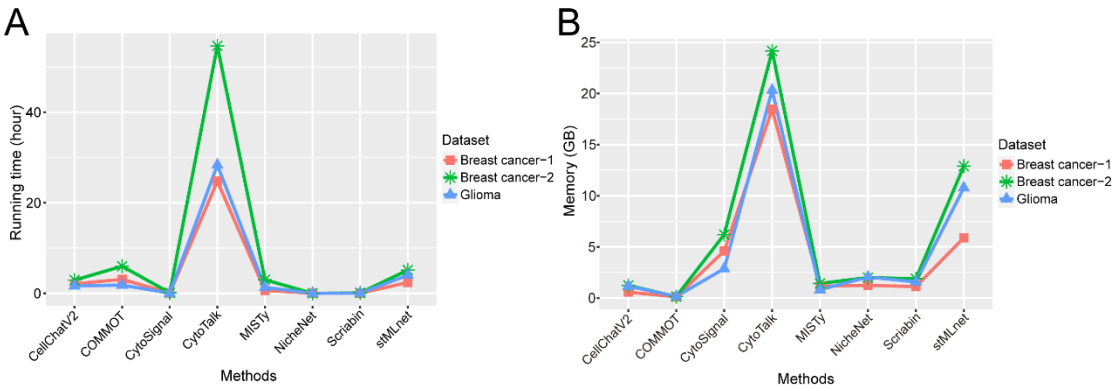

Figure S4. Comparison of computing resource among the CCC inference methods. (A) Line chart of running time of the methods on different datasets. (B) Line chart of memory usage of the methods on different data sets.

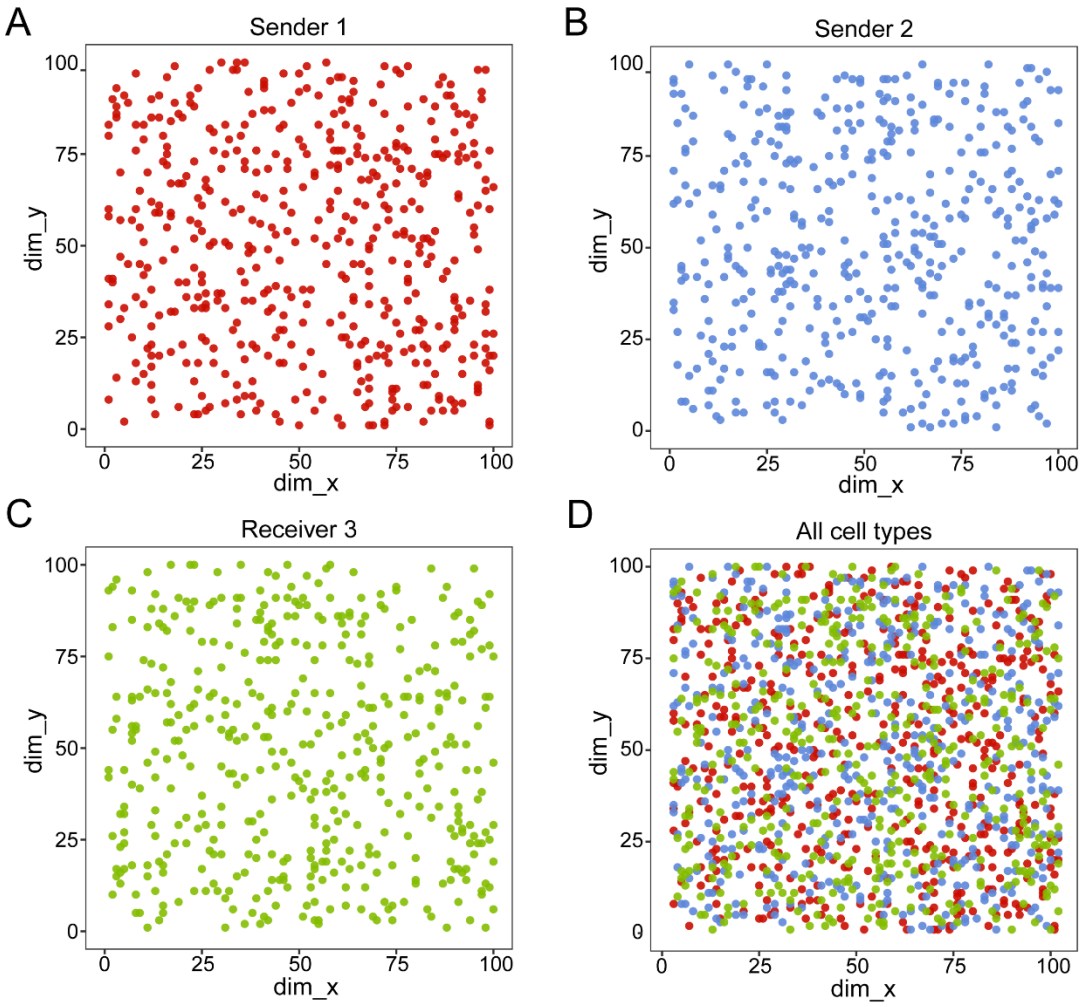

Figure S5. Spatial distribution of cell types in simulation dataset 1. (A) The spatial distribution of Sender 1 is randomly generated. (B)The spatial distribution of Sender 2 is randomly generated. (C) The spatial distribution of Receiver 3 is randomly generated. (D) The spatial distribution of all cell types.

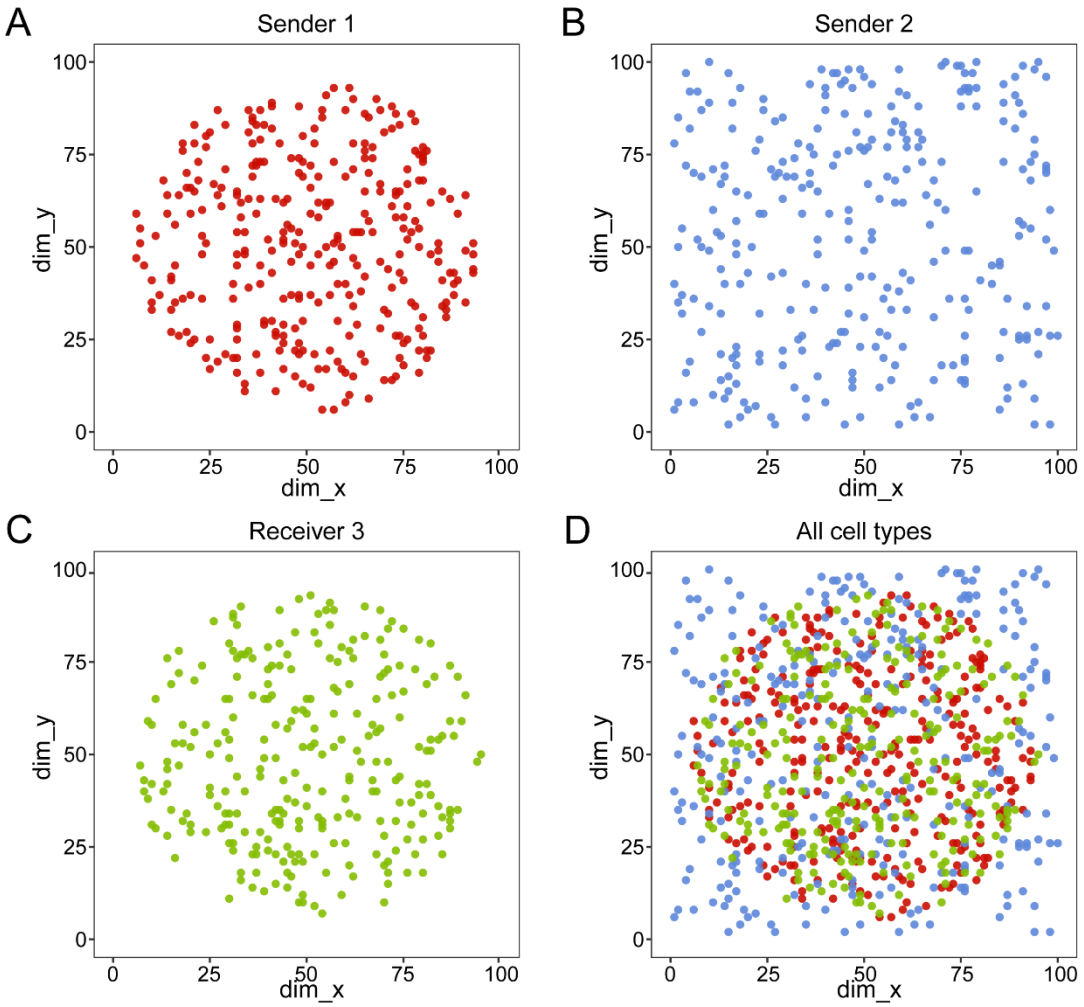

Figure S6. Spatial distribution of cell types in simulation dataset 2. (A) The spatial distribution of Sender 1 is randomly generated in a circular region. (B) The spatial distribution of Sender 2 is randomly distributed in the entire square domain. (C) The spatial distribution of Receiver 3 is randomly generated in circular region. (D) The spatial distribution of all cell types.

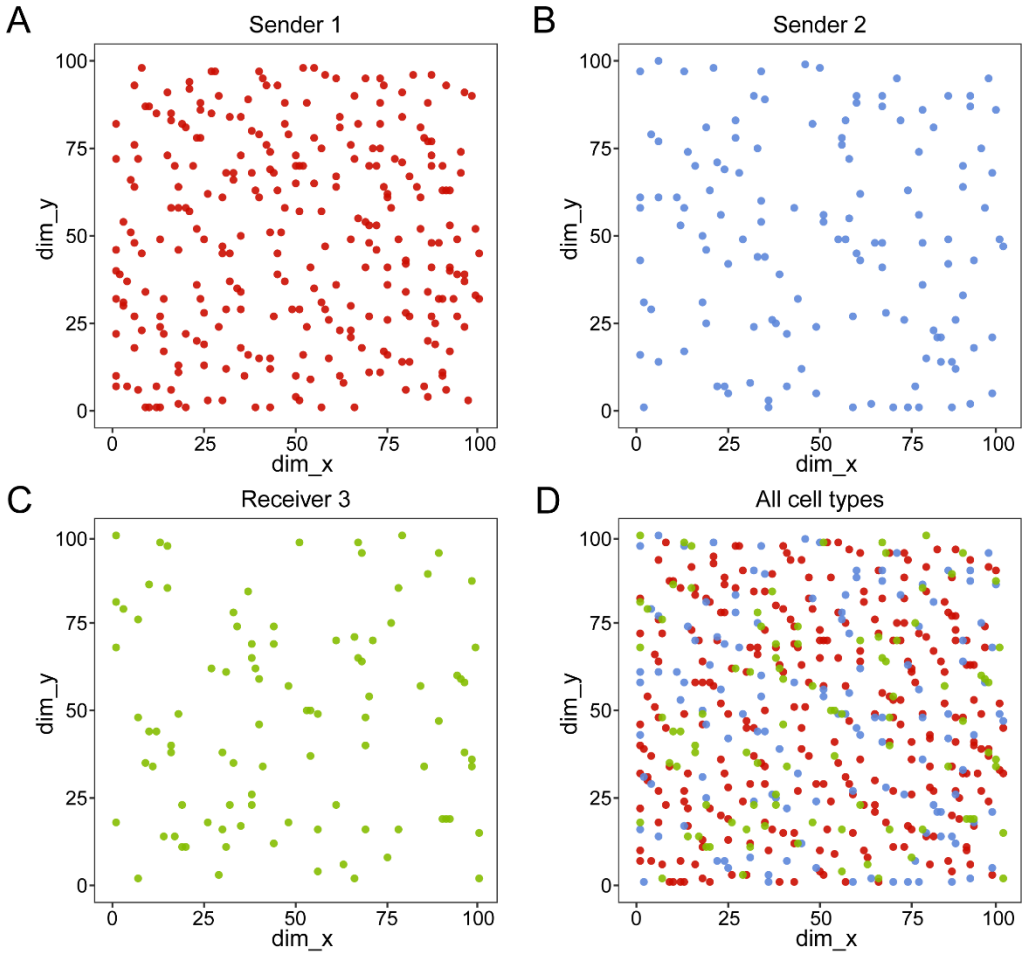

Figure S7. Spatial distribution of cell types in simulation dataset 3. (A) The spatial distribution of Sender 1 is randomly generated. (B) The spatial distribution of Sender 2 is randomly generated. (C) The spatial distribution of Receiver 3 is randomly generated. (D) The spatial distribution of all cell types. Some cells in Sender 1, Sender 2, and Receiver 3 were simulated to share the same spatial position, mimicking spatial embedding where true cell position is rasterized by a synthetic microarray (e.g., Visium or SlideSeq arrays).

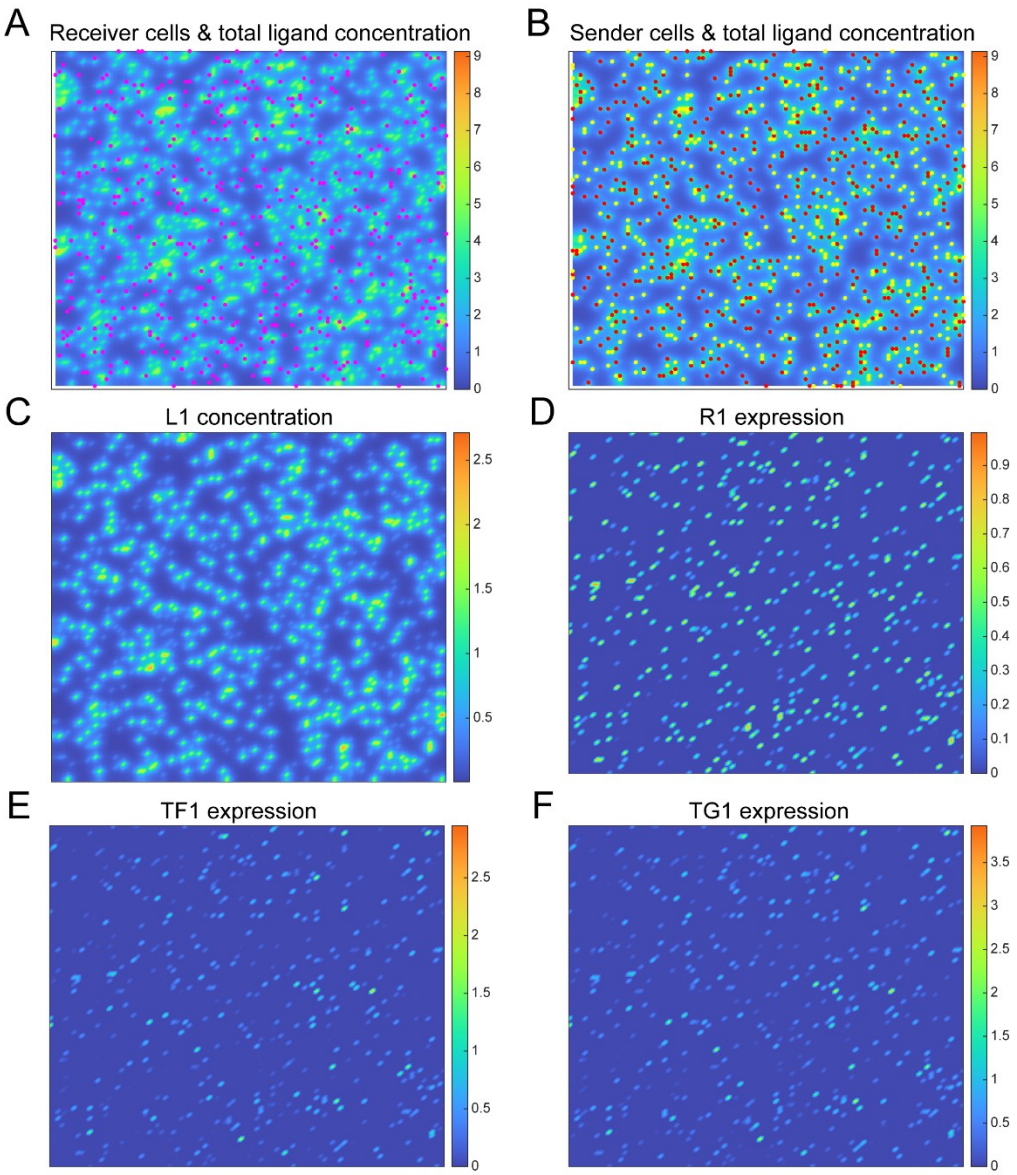

Figure S8. Illustration of the simulation study for simulation data 1. (A-F) a representative simulation realized with a set of randomly sampled parameters. Shown are spatial distributions of receiver cells (A) and sender cells (red for Sender 1 and yellow for Sender 2) (B) with total ligand concentration as background, L1 concentration (C), R1 expression (D), TF1 activation (E), and TG1 expression (F), respectively.

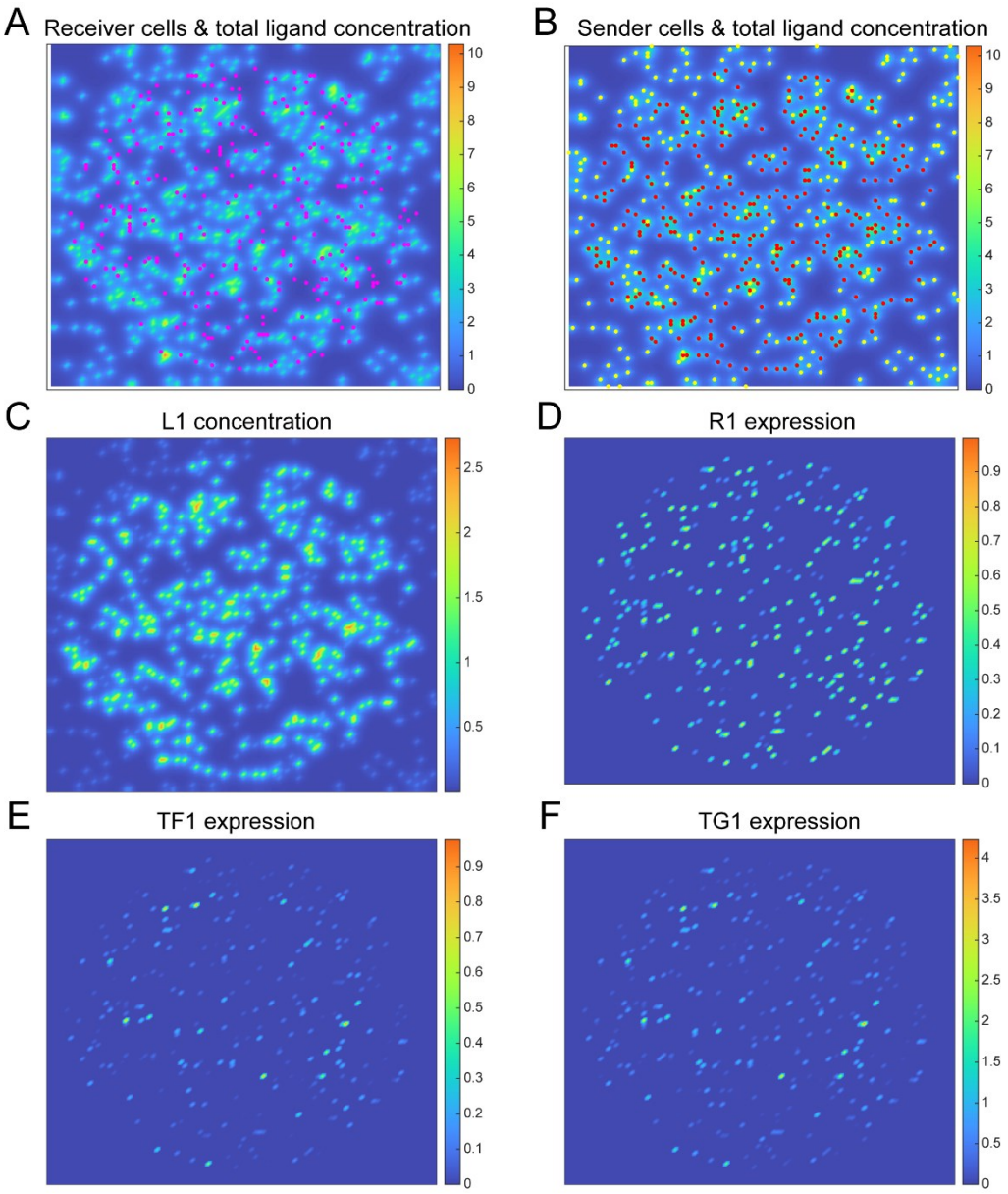

Figure S9. Illustration of the simulation study for simulation data 2. (A-F) a representative simulation realized with a set of randomly sampled parameters. Shown are spatial distributions of receiver cells (A) and sender cells (red for Sender 1 and yellow for Sender 2) (B) with total ligand concentration as background, L1 concentration (C), R1 expression (D), TF1 activation (E) and, TG1 expression (F), respectively.

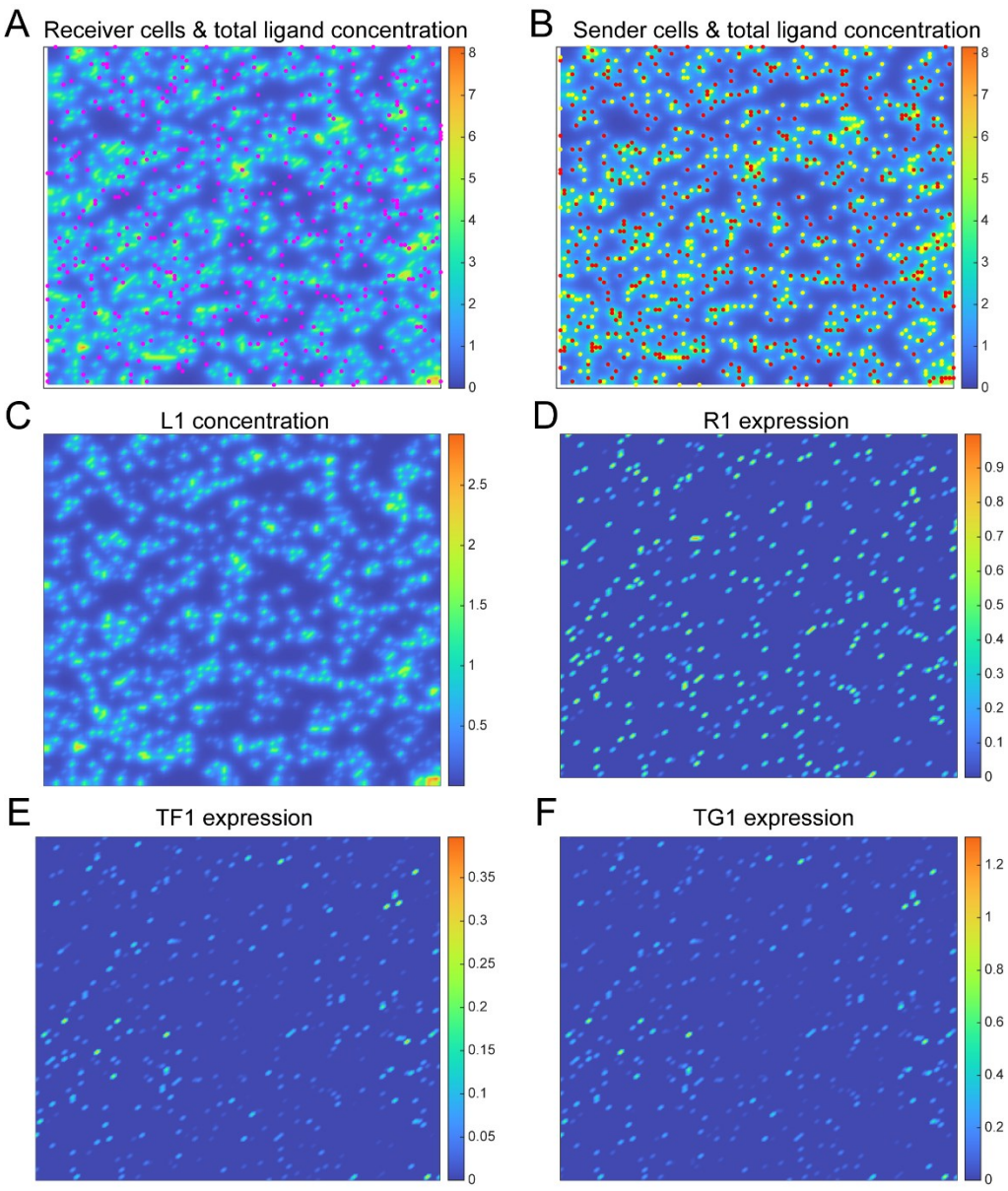

Figure S10. Illustration of the simulation study for simulation data 3. (A-F) a representative simulation realized with a set of randomly sampled parameters. Shown are spatial distributions of receiver cells (A) and sender cells (red for Sender 1 and yellow for Sender 2) (B) with total ligand concentration as background, L1 concentration (C), R1 expression (D), TF1 activation (E) and TG1 expression (F), respectively.

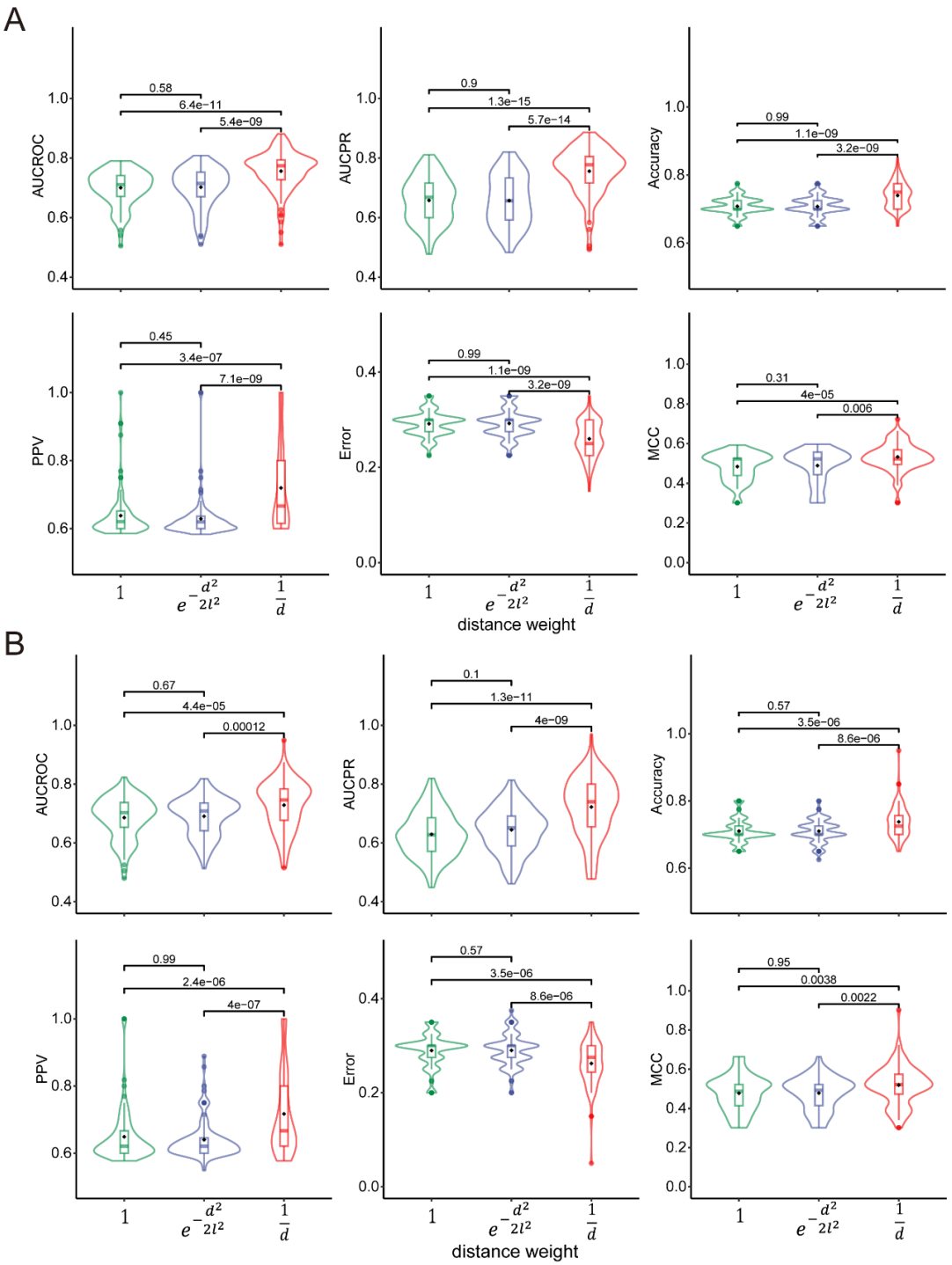

Figure S11. The performance of stMLnet with the reciprocal weighting function and two variants. Based on simulation dataset 2 (A) and simulation dataset 3 (B), the performances of stMLnet with the reciprocal weighting function and the two variants in predicting LR-TG regulation were evaluated and compared. The Wilcoxon rank sum test p value was used to assess the statistical significance. AUROC: area under the ROC curve, AUPRC: area under the Precision/Recall curve, PPV: positive predictive value, MCC: Matthews correlation coefficient.

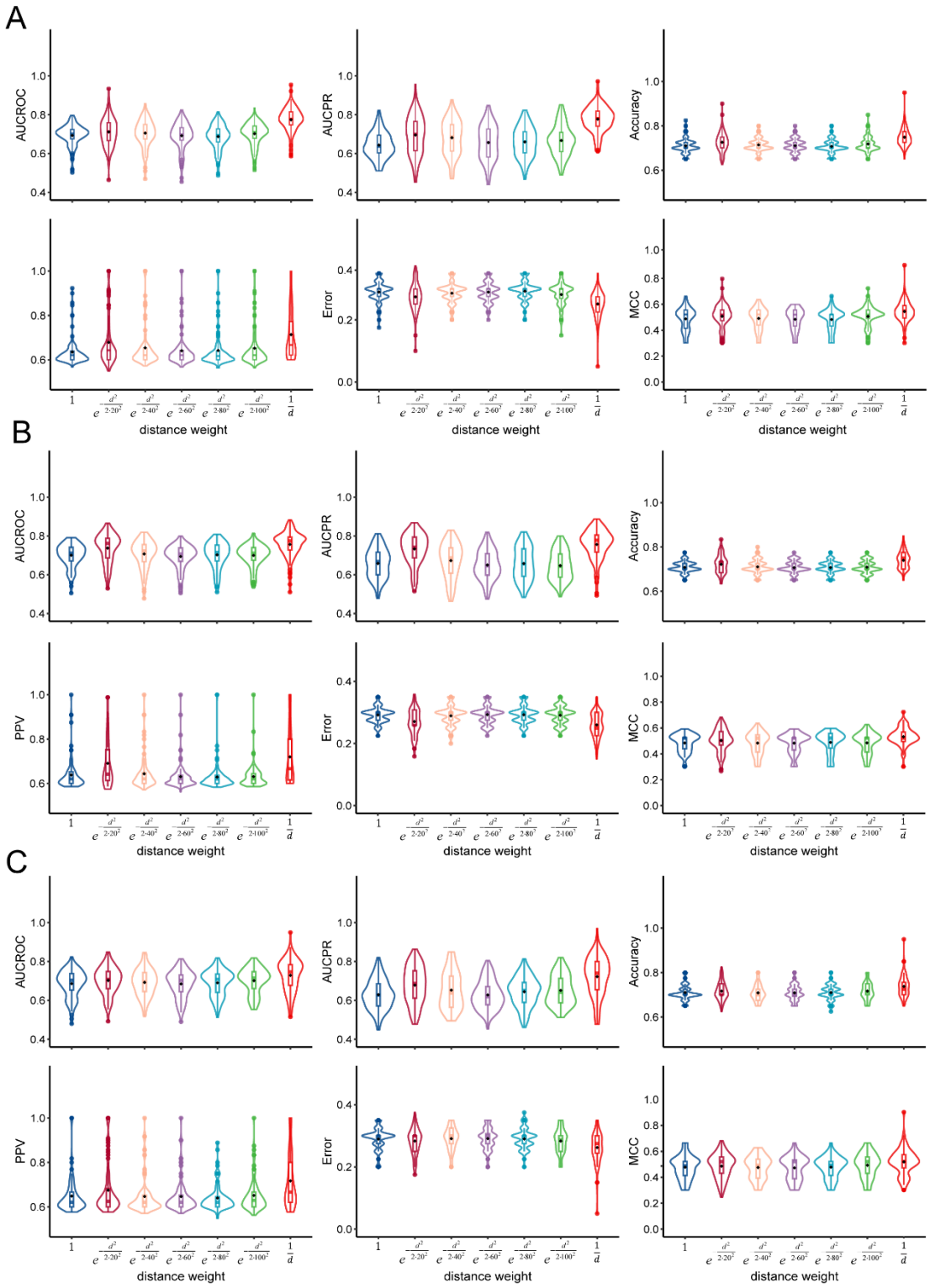

Figure S12. Evaluation and comparison of the effect of the hyperparameter l on the performance of stMLnet when using the radial basis function as the weight function. Based on three simulation datasets, the performances of stMLnet with the reciprocal weighting function and the two variants in predicting LR-TG regulation were evaluated and compared. In particular, different values of l (i.e., $l = 20, 40, 60, 80, 100$) were compared when using radial basis functions as weighting functions. Shown are the comparison results on the simulation dataset 1 (A), the simulation dataset 2 (B), and the simulation dataset 3 (C), respectively.

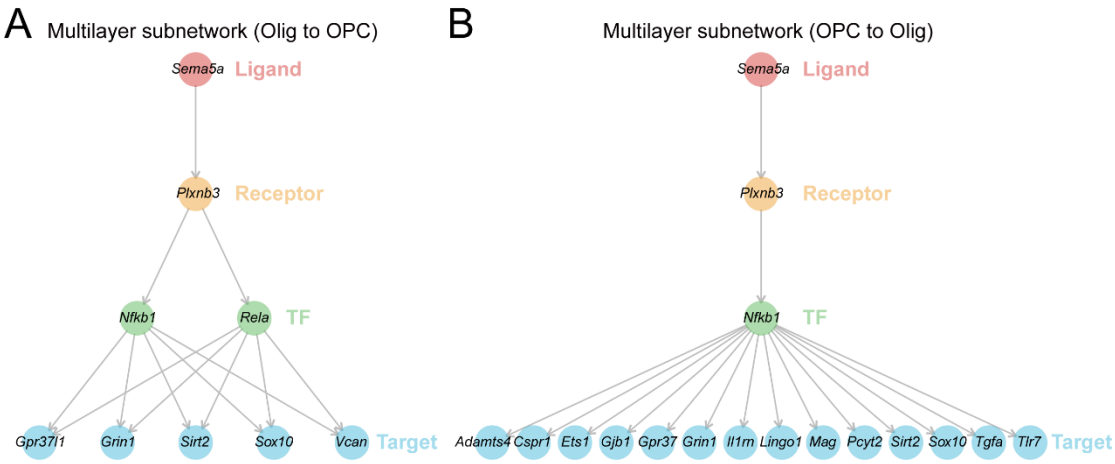

Figure S13. The multilayer signaling subnetwork between Olig and OPC in seqFISH+ data. (A) Multilayer signaling subnetwork from Olig to OPC. (B) Multilayer signaling subnetwork from OPC to Olig.

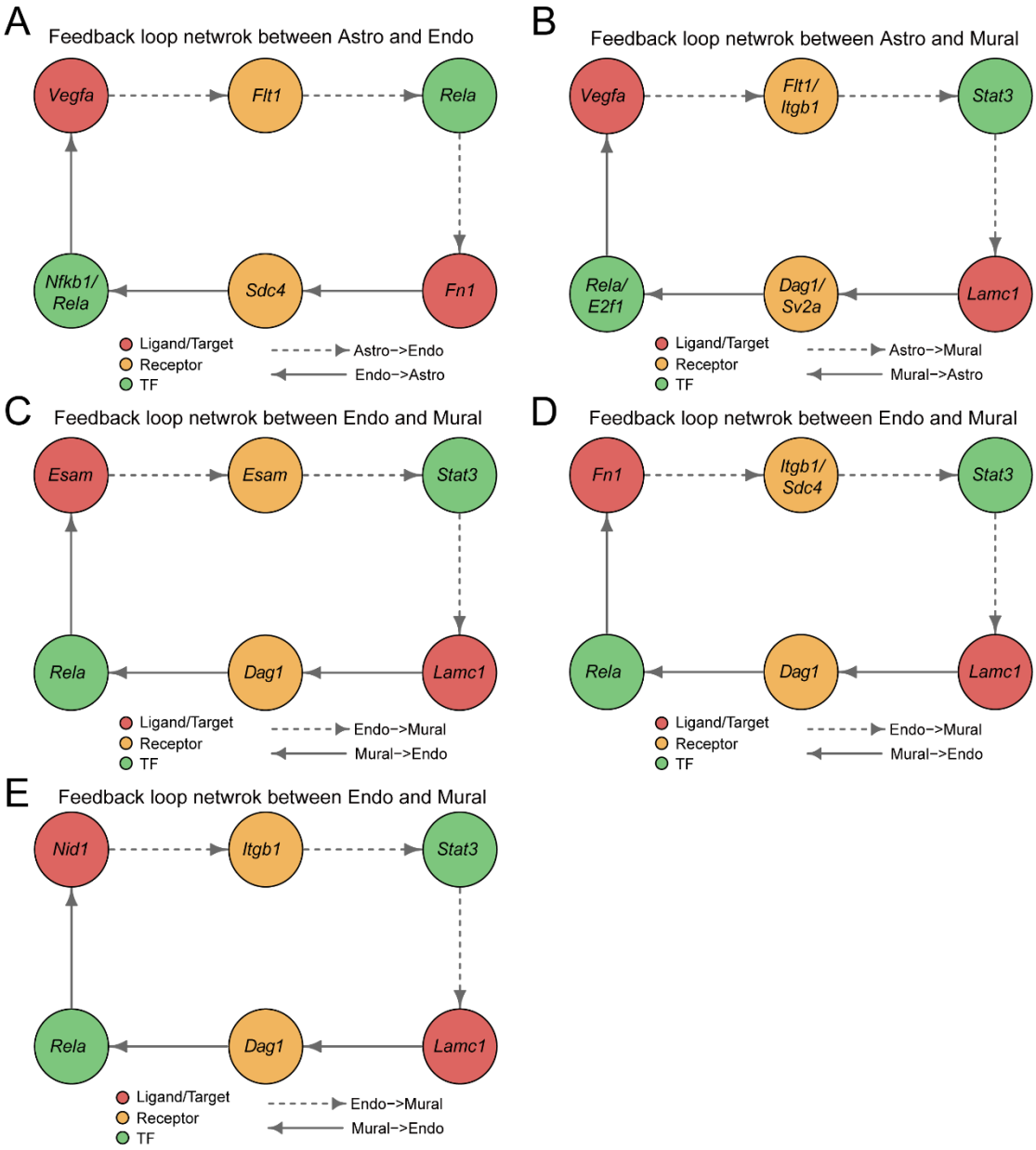

Figure S14. The feedback loop networks between Astro, Endo, and Mural. (A) The feedback loop between Astro and Endo. Solid arrows represent signaling from Endo to Astro, while dashed arrows indicate signaling from Astro to Endo. The red nodes, yellow nodes, and green nodes represent the ligand/target gene, receptor, and TF, respectively. Ligand *Vegfa* interacts with receptor *Flt1*, while ligand *Fn1* interacts with receptor *Sdc4*. Additionally, *Vegfa* is a downstream target of receptor *Sdc4* via TFs *Nfkb1/Rela*. Similarly, *Fn1* is a downstream target of *Flt1* through TF *Rela*. (B) The feedback loop between Astro and Mural. Solid arrows indicate signaling from Mural to Astro, while dashed arrows represent signaling from Astro to Mural. Ligand *Vegfa* interacts with receptors *Flt1/Itgb1*, while ligand *Lamc1* interacts with receptors *Dag1/Sv2a*. Additionally, *Vegfa i*s a downstream target of receptors *Dag1/Sv2a* via TFs *Rela/E2f1*. Similarly, *Lamc1* is a downstream target of receptors *Flt1/Itgb1* through TF *Stat3*. (C-E) The feedback loop between Endo and Mural. Solid arrows indicate signaling from Mural to Endo, while dashed arrows represent signaling from Endo to Mural. (C) Ligand *Esam* interacts with receptor *Esam*, while ligand *Lamc1* interacts with receptor *Dag1*. Additionally,

Esam is a downstream target of receptor *Dag1* via TF *Rela*. Similarly, *Lamc1* is a downstream target of receptor *Esam* through TF *Stat3*. (D) Ligand *Fn1* interacts with receptors *Itgb1/Sdc4*, while ligand *Lamc1* interacts with receptor *Dag1*. Additionally, *Fn1* is a downstream target of receptor *Dag1* via TF *Rela*. Similarly, *Lamc1* is a downstream target of receptors *Itgb1/Sdc4* through TF *Stat3*. (E) Ligand *Nid1* interacts with receptor *Itgb1*, while ligand *Lamc1* interacts with receptor *Dag1*. Additionally, *Nid1* is a downstream target of receptor *Dag1* via TF *Rela*. Similarly, *Lamc1* is a downstream target of receptor *Itgb1* through TF *Stat3*.

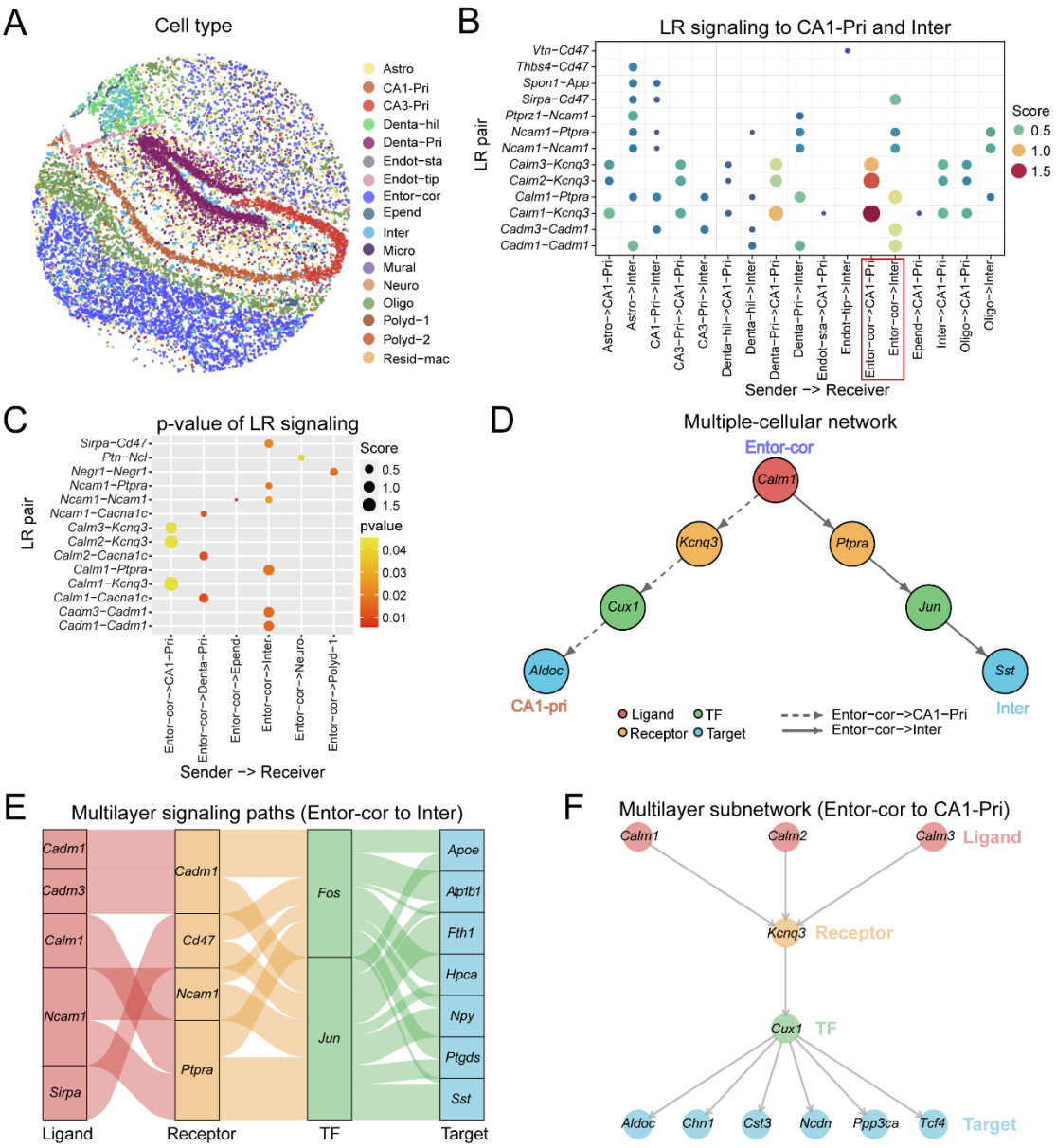

Figure S15. Multilayer signaling analysis of inferred CCC in Slide-seqV2 data using stMLnet. (A) Spatial distribution of Slide-seqV2 of mouse hippocampus. Astro: Astrocyte; CA1-Pri: CA1-Principal; CA3-Pri: CA3-Principal; Denta-hil: Dentate-hilum; Denta-Pri: Dentate-Principal; Endot-sta: Endothelial-stalk; Endot-tip: Endothelial-tip; Endot-cor: Entorhinal-cortex; Epend: Ependymal; Inter: Interneuron; Micro: Microglia; Neuro: Neurogenesis; Oligo: Oligodendrocyte; Polyd-1: Polydendrocyte-1; Polyd-2: Polydendrocyte-2; Resid-mac: Resident-macrophage. (B) Bubble plot of inferred LR signaling activity from other cell types to CA1-Pri and Inter. "Score" denotes the LR signaling activity. The LR signaling score greater than 0.05 were plotted for visualization. (C) Heatmap plot of significant LR pairs from Entor-cor to other cell groups. Circle size is proportional to the LR signaling activity, and color represents p-values. (D) Multi-cellular network delineates the regulatory mechanisms by which Entor-cor cells interact with Inter cells and CA1-Pri cells through ligand signaling of *Calm1*. (E) Waterfall plot of multilayer signaling network from Entor-cor to Inter. The thickness of flow indicates the contribution of the LR pair to the downstream TG. (F) Multilayer signaling subnetwork from

Entor-cor to CA1-Pri. (E-F) can clearly show the multilayer signaling regulation pathway (L-R-TF-TG) from sender cell to receiver cell.

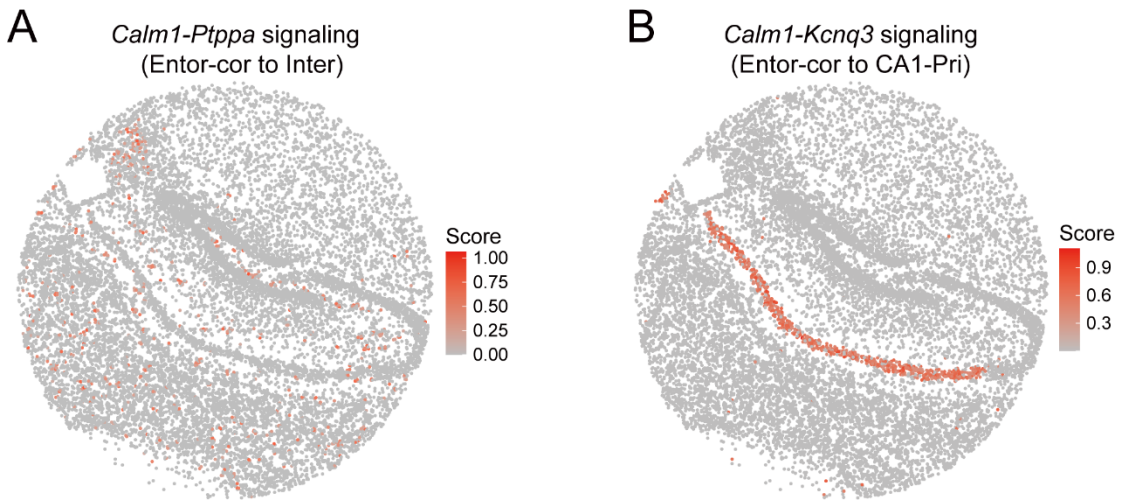

Figure S16. The spatial distribution of specific LR signaling score in the Slide-seq v2 dataset. (A) The spatial distribution of *Calm1-Ptppa* signaling score from Entor-cor to Inter. (B) The spatial distribution of *Calm1-Kcnq3* signaling score from Entor-cor to CA1-Pri.

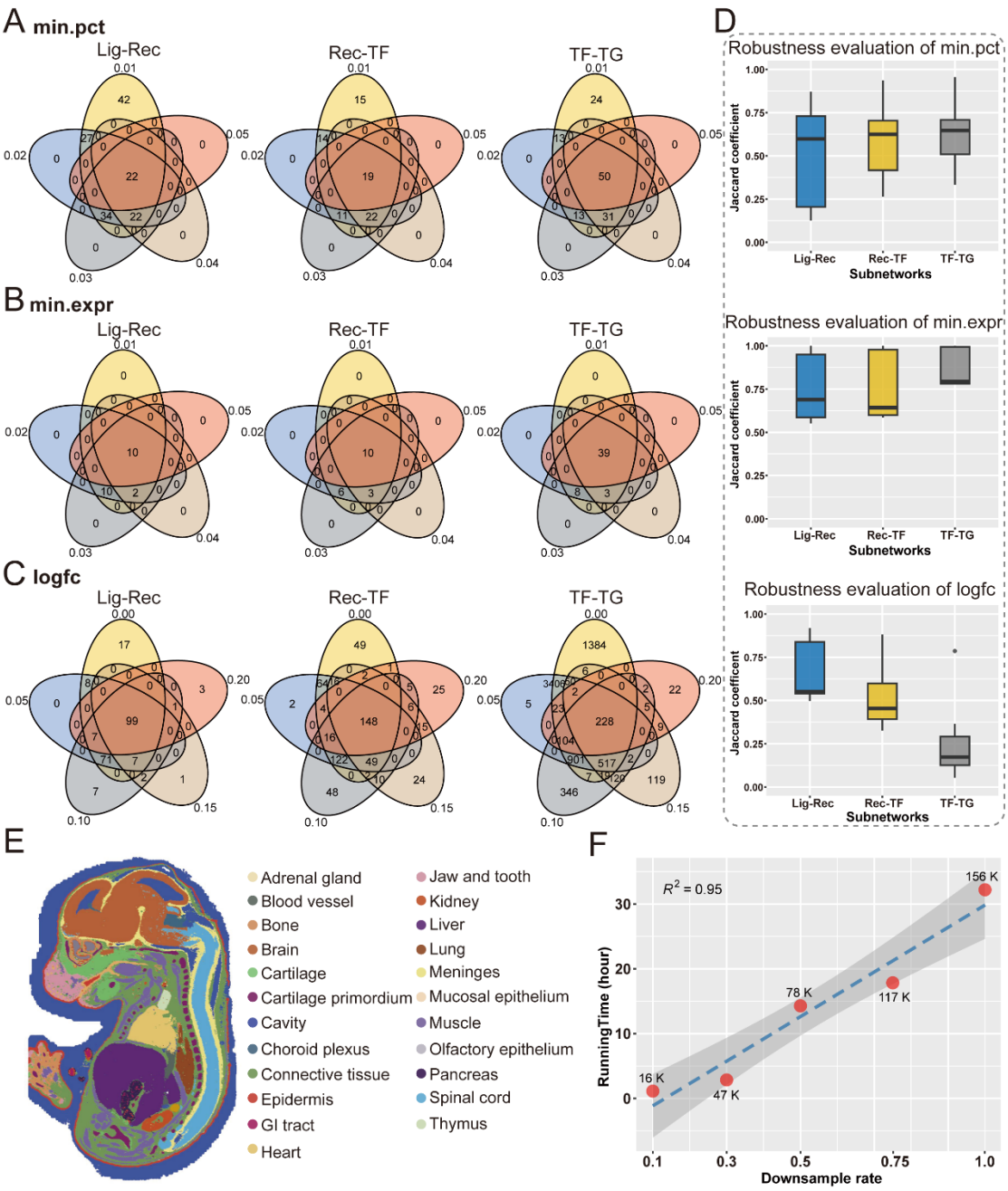

Figure S17. Evaluation of robustness and scalability of stMLnet. (A-D) The robustness of stMLnet was evaluated on Slide-seq V2 data. Venn diagram shows intersections between subnetworks (i.e., Lig-Rec, Rec-TF, TF-TG) inferred by stMLnet under different min.pct settings (A), different min.expr settings (B), and different logfc settings (C). Different colors correspond to different values of each tested parameter. (D) Robustness evaluation of stMLnet using Jaccard coefficient. Multilayer networks were inferred by stMLnet with different parameter values. Jaccard coefficient was calculated to assess the consistence between the inferred subnetworks (i.e., Lig-Rec, Rec-TF, or TF-TG) with respect to any two different parameter combinations. The larger the Jaccard coefficient value, the more similar the two sets are. (E-F) Scalability of stMLnet assessed using a large-scale ST dataset. (E) Spatial distribution of cells in Stereo-seq data of mouse embryo in E16.5 section. (F) Running time of stMLnet on a series of down-sampled Stereo-seq datasets. The number next to each point represents the number

of cells corresponding to each down-sampling rate, and the blue dashed line represents the linear regression fit to these points.

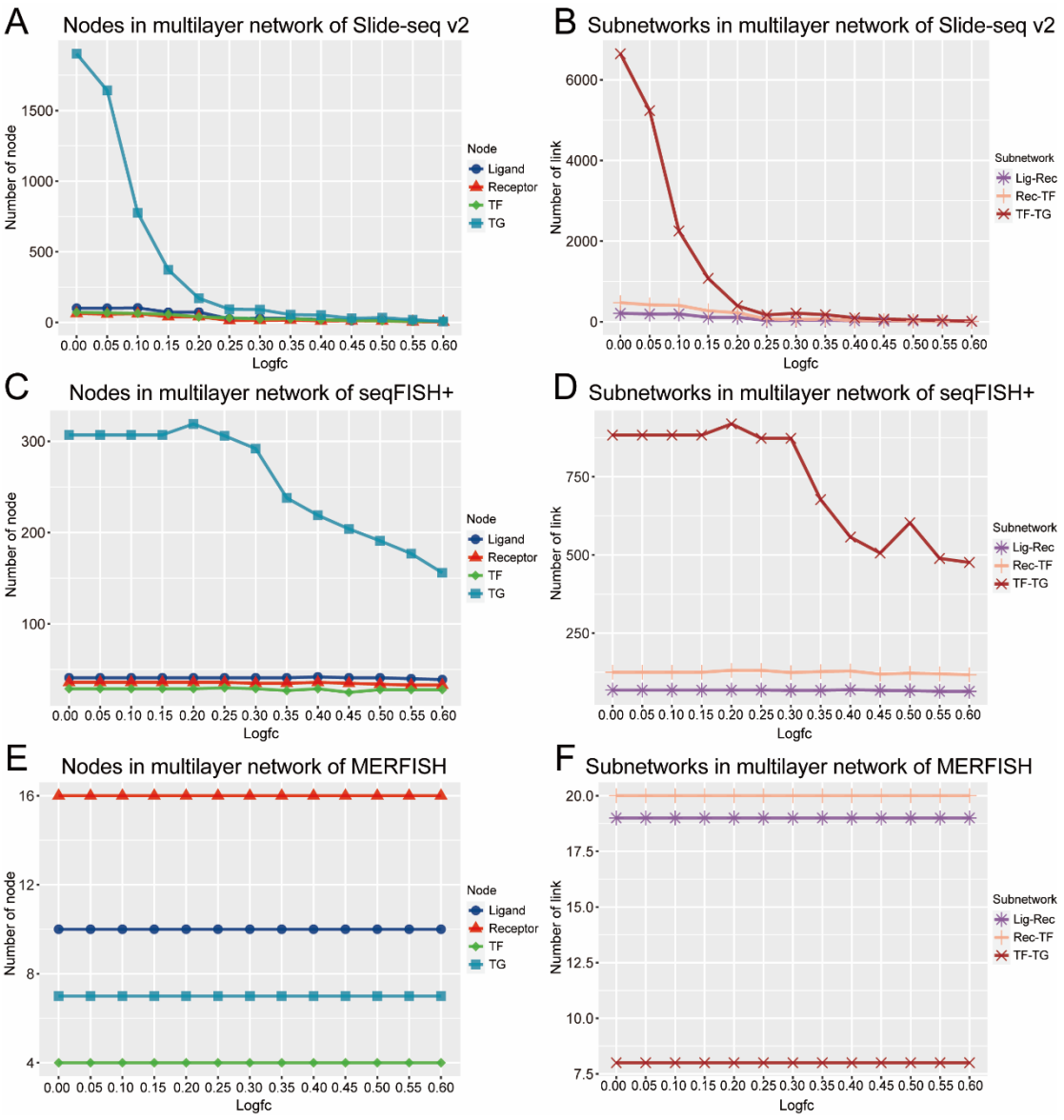

Figure S18. Evaluation of robustness of stMLnet about logfc on three ST datasets. (A) Line plot shows the number of nodes in the multilayer network corresponding to different logfc parameter settings in Slide-seq v2 data. (B) Line plot shows the number of links in the three subnetworks corresponding to different logfc parameter settings in Slide-seq v2 data. (C) Line plot shows the number of nodes in the multilayer network corresponding to different logfc parameter settings in seqFISH+ data. (D) Line plot shows the number of links in the three subnetworks corresponding to different logfc parameter settings in seqFISH+ data. (E) Line plot shows the number of nodes in the multilayer network corresponding to different logfc parameter settings in MERFISH data. (F) Line plot shows the number of links in the three subnetworks corresponding to different logfc parameter settings in MERFISH data.

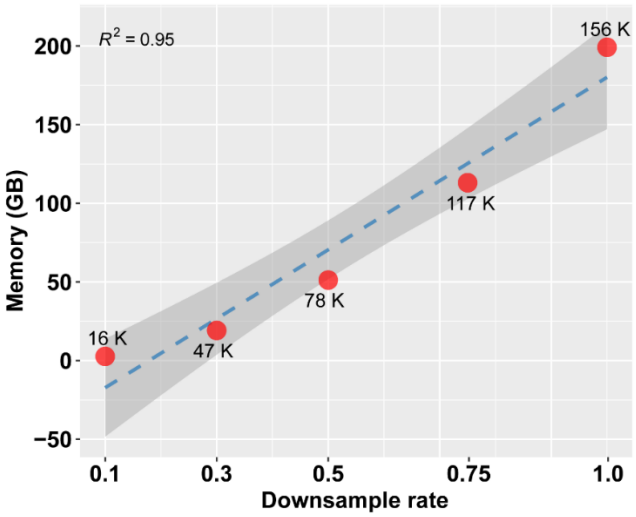

Figure S19. Memory usage of stMLnet on a series of down-sampled Stereo-seq datasets. The number next to each point represents the number of cells corresponding to each down-sampling rate, and the blue dashed line represents the linear regression fit to these points.

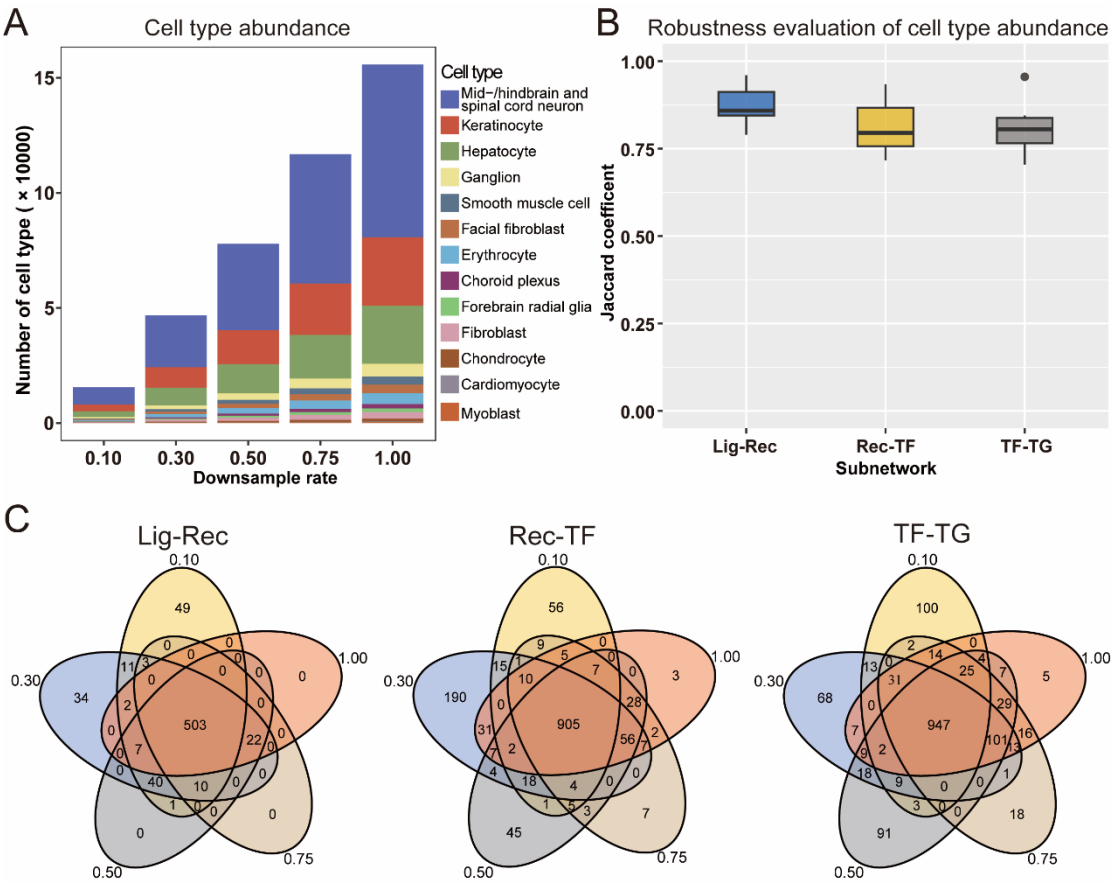

Figure S20. Evaluation of robustness of stMLnet to cell type abundance. (A) Bar plot illustrates the distribution of cell type in the dataset with different down-sampling rates. Different colors represent different cell types. (B) Robustness evaluation of stMLnet with respect to cell type abundance using Jaccard coefficient. Multilayer networks were inferred by stMLnet from datasets with different down-sampling rates. Jaccard coefficient was calculated to assess the consistence between the inferred subnetworks (i.e., Lig-Rec, Rec-TF, or TF-TG) with respect to any two different down-sampling rates. The larger the Jaccard coefficient value, the more similar the two subnetworks are. (C) Venn diagram shows intersections between subnetworks (i.e., Lig-Rec, Rec-TF, TF-TG) inferred by stMLnet under different down-sampling rates. Different colors correspond to different down-sampling rates.

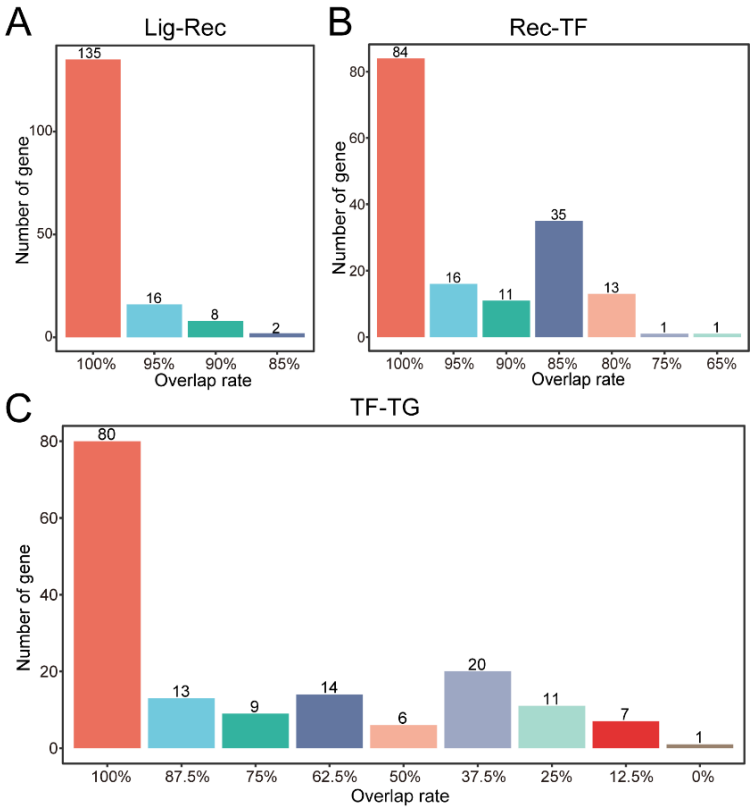

Figure S21. Evaluation of the robustness of stMLnet to gene dropout on the MERFISH dataset. The bar plot illustrates the number of genes corresponding to the three subnetworks at various overlap rates. The overlap rate represents the extent of similarity between the subnetwork after the sequential dropout of 161 genes (one at a time) and the original subnetwork without dropout. An overlap rate of 100% indicates that the subnetwork remains identical to the original even after a specific gene is dropped out. The number displayed above each bar represents the number of genes associated with each overlap rate. Panels (A), (B), and (C) illustrate the number of genes corresponding to the Lig-Rec, Rec-TF, and TF-TG subnetworks at various overlap rates, respectively.

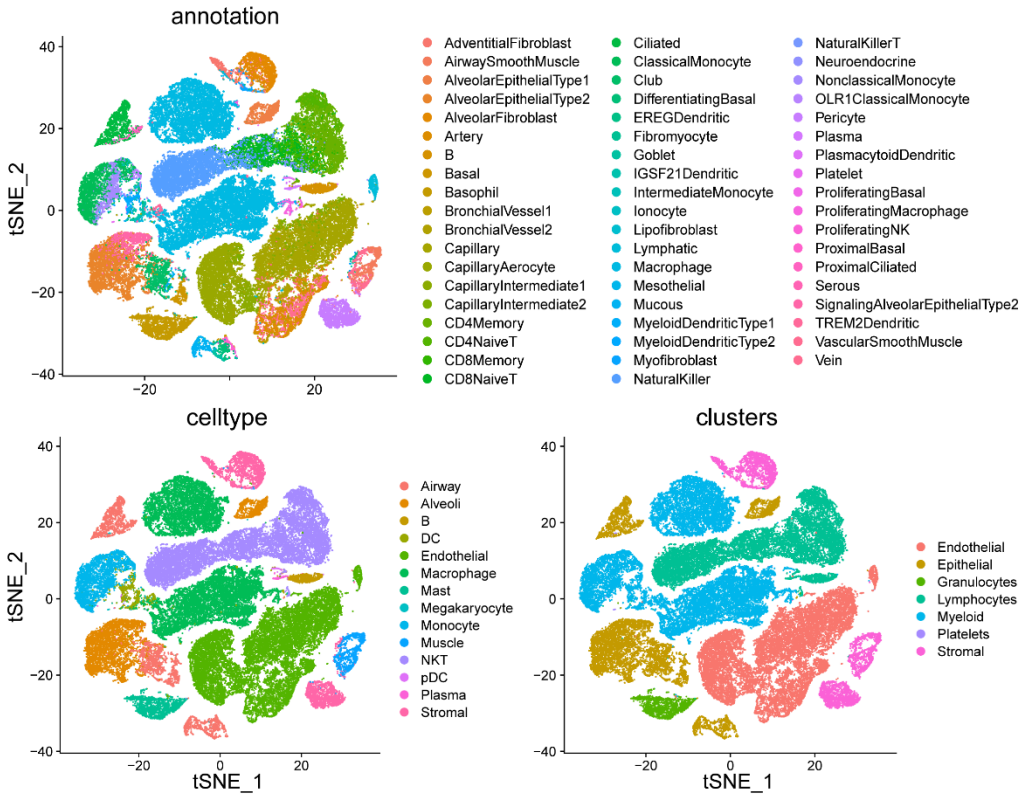

Figure S22. The cell type annotation for the scRNA-seq data of COVID-19. Shown are TSNE of expression profile of scRNA-seq data from views of annotations, cell types and clusters.

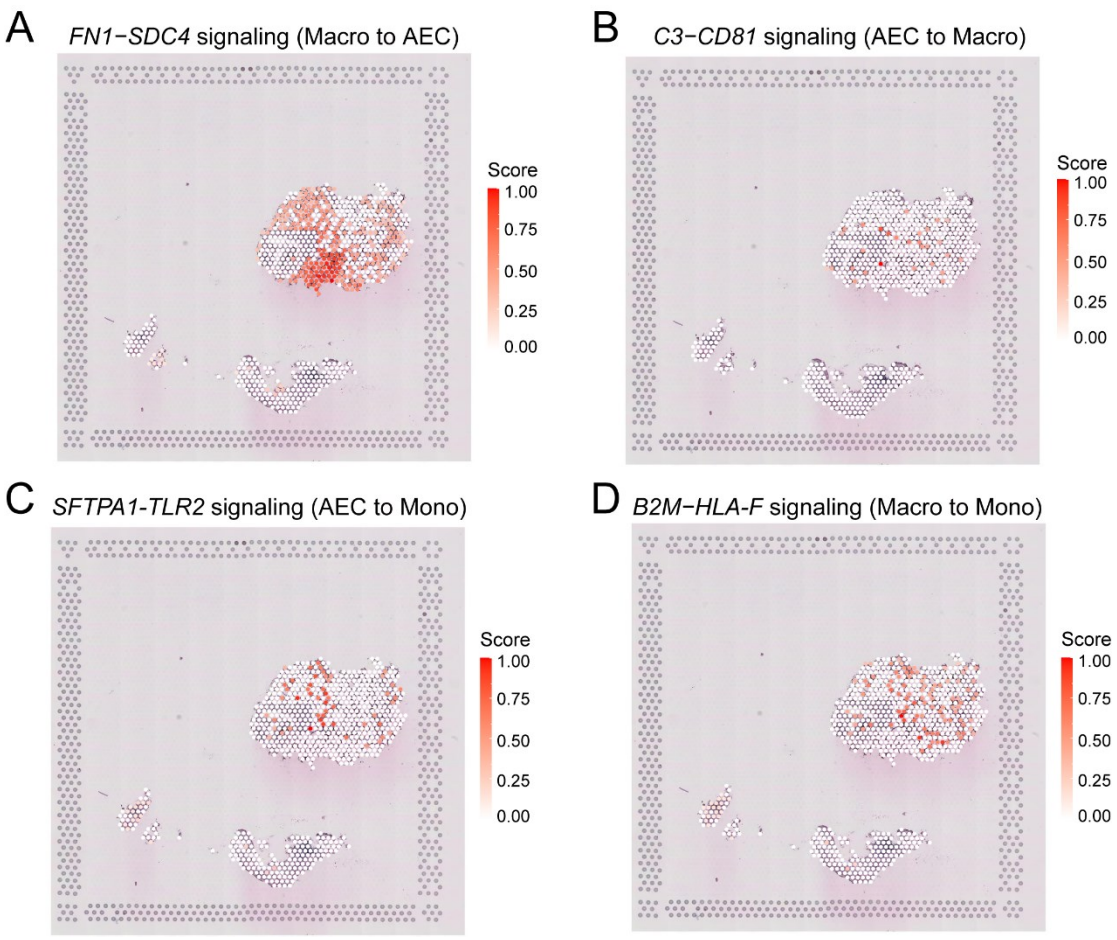

Figure S23. The spatial distribution of specific LR signaling score in the COVID-19 dataset. (A) The spatial distribution of *FN1-SDC4* signaling score from Macro to AEC. (B) The spatial distribution of *C3-CD81* signaling score from AEC to Macro. (C) The spatial distribution of *SFTPA1-TLR2* signaling score from AEC to Mono. (D) The spatial distribution of *B2M-HLA-F* signaling score from Macro to Mono.

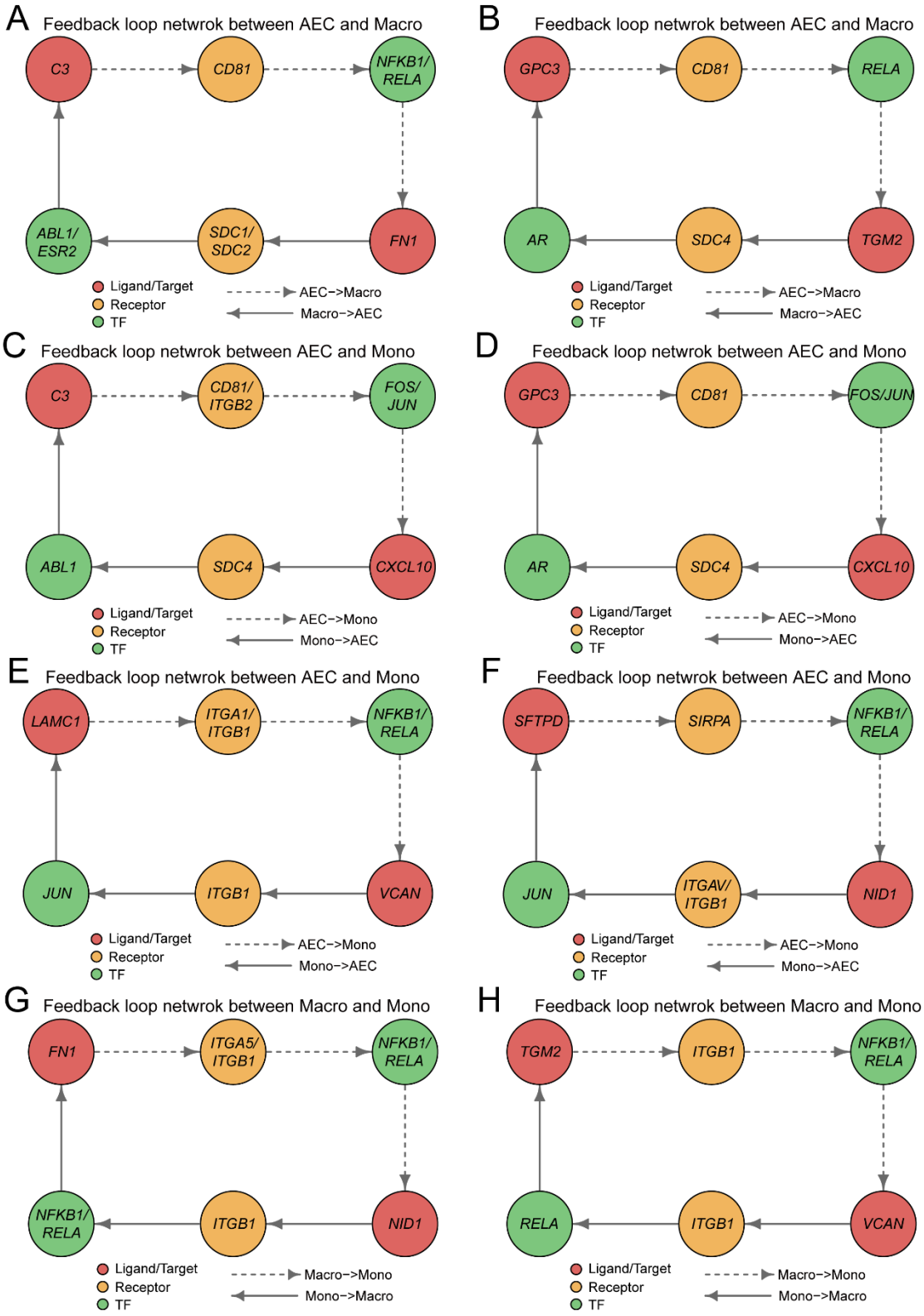

Figure S24. The feedback loop networks between AEC, Macro, and Mono. (A-B) The feedback loop between AEC and Macro. Dashed arrows represent signaling from AEC to Macro, while solid arrows indicate signaling from Macro to AEC. The red nodes, yellow nodes, and green nodes represent the ligand/target gene, receptor, and TF, respectively. (A) ligand *C3* interacts with receptor *CD81*, while ligand *FN1* interacts with receptors *SDC1/SDC2*.

Additionally, *C3* is a downstream target of receptors *SDC1/SDC2* via TFs *NFKB1/RELA*. Similarly, *FN1* is a downstream target of receptor *CD81* through TFs *NFKB1/RELA*. (B) ligand *GPC3* interacts with receptor *CD81*, while ligand *TGM2* interacts with receptor *SDC4*. Additionally, *GPC3* is a downstream target of receptor *SDC4* via TF *AR*. Similarly, *TGM2* is a downstream target of receptor *CD81* through TF *RELA*. (C-F) The feedback loop between AEC and Mono. Dashed arrows represent signaling from AEC to Mono, while solid arrows indicate signaling from Mono to AEC. (C) ligand *C3* interacts with receptors *CD81/ITGB2*, while ligand *CXCL10* interacts with receptors *SDC4*. Additionally, *C3* is a downstream target of receptors *SDC4* via TF *ABL1*. Similarly, *CXCL10* is a downstream target of receptors *CD81/ITGB2* through TFs *FOS/JUN*. (D) ligand *GPC3* interacts with receptors *CD81*, while ligand *CXCL10* interacts with receptor *SDC4*. Additionally, *GPC3* is a downstream target of receptors *SDC4* via TF *AR*. Similarly, *CXCL10* is a downstream target of receptors *CD81* through TFs *FOS/JUN*. (E) ligand *LAMC1* interacts with receptors *ITGA1/ITGB1*, while ligand *VCAN* interacts with receptor *ITGB1*. Additionally, *LAMC1* is a downstream target of receptors *ITGB1* via TF *JUN*. Similarly, *VCAN* is a downstream target of receptors *ITGA1/ITGB1* through TFs *NFKB1/RELA*. (F) ligand *SFTPD* interacts with receptors *SIRPA*, while ligand *NID1* interacts with receptor *ITGAV/ITGB1*. Additionally, *SFTPD* is a downstream target of receptors *ITGAV/ITGB1* via TF *JUN*. Similarly, *NID1* is a downstream target of receptors *SIRPA* through TFs *NFKB1/RELA*. (G-H) The feedback loop between Macro and Mono. Dashed arrows represent signaling from Macro to Mono, while solid arrows indicate signaling from Mono to Macro. (G) ligand *FN1* interacts with receptors *ITGA5/ITGB1*, while ligand *NID1* interacts with receptor *ITGB1*. Additionally, *FN1* is a downstream target of receptors *ITGB1* via TFs *NFKB1/RELA*. Similarly, NID1 is a downstream target of receptors *ITGA5/ITGB1* through TFs *NFKB1/RELA*. (H) ligand *TGM2* interacts with receptor *ITGB1*, while ligand *VCAN* interacts with receptor *ITGB1*. Additionally, *TGM2* is a downstream target of receptors *ITGB1* via TF *RELA*. Similarly, *VCAN* is a downstream target of receptor *ITGB1* through TFs *NFKB1/RELA*.

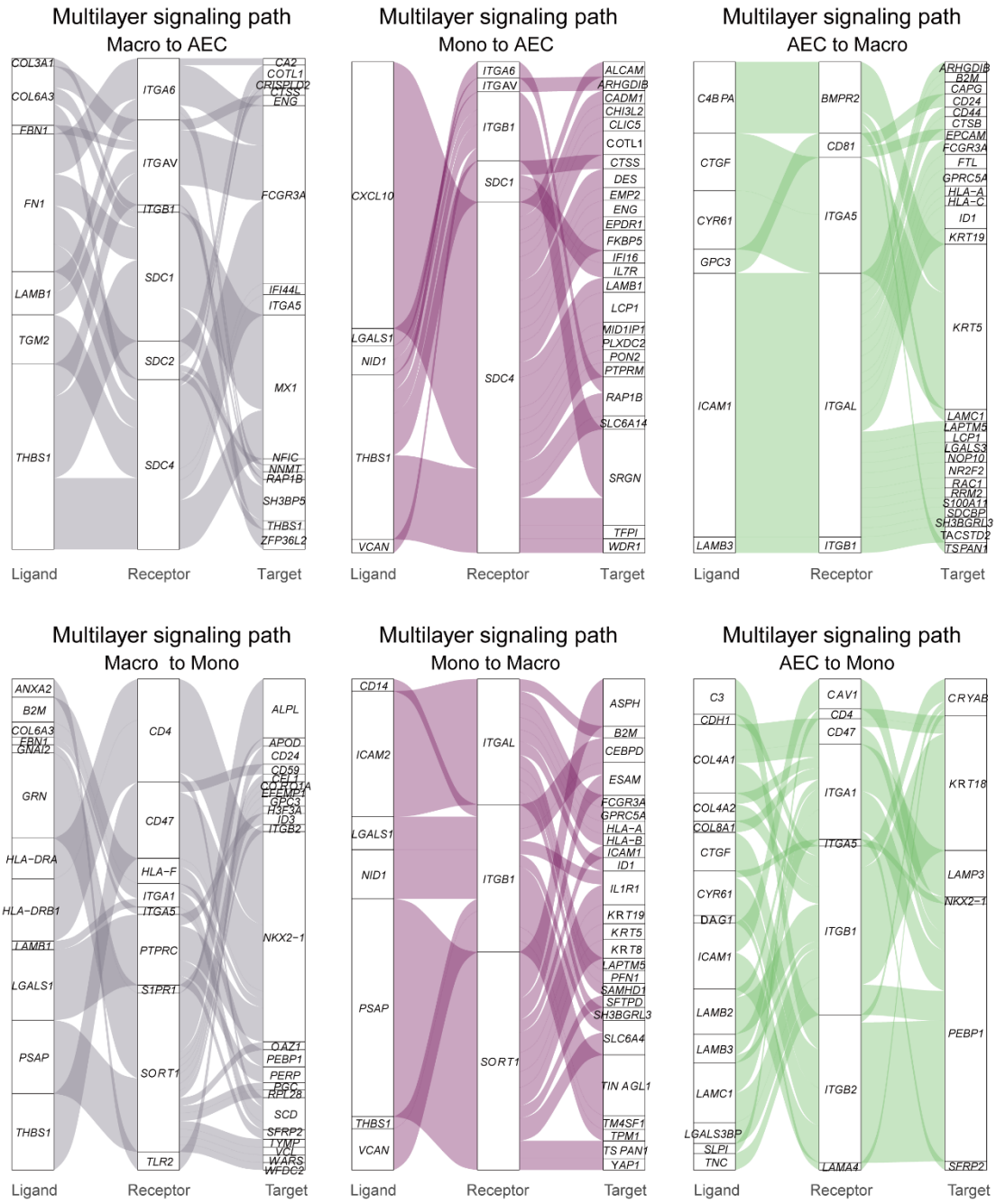

Figure S25. **The waterfall plot of the multilayer signaling network for the cellular feedback circuits inferred from the COVID-19 ST dataset.** Shown are regulatory paths from upstream LR pairs (top ranked) to their downstream targets for each pair of cell types among AEC, macrophages, and monocytes. Different colors of paths represent cellular source (sender cells) of the ligand signaling, and width of the path represents the importance score of each LR~TG regulation.

Figure S26. Heatmap of functional enrichment for cellular feedback circuits inferred from the COVID-19 ST dataset. Shown are GO biological process (up) or KEGG (below) enrichment results of the intracellular target genes downstream of the upstream receptors involved in the multilayer networks for feedback circuits among AEC, Macro and Mono. Top ranked gene terms according to p values were prioritized for visualization.

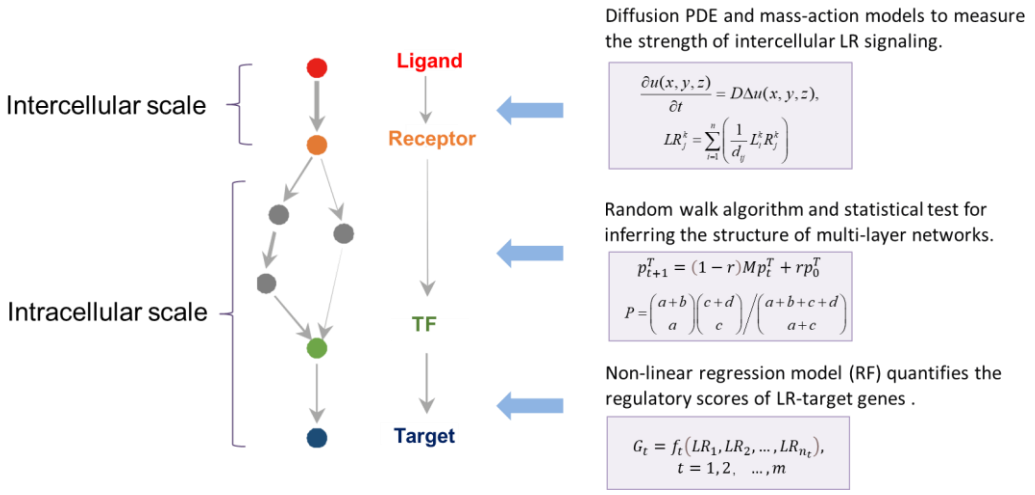

Figure S27. A unified framework for multiscale inference of spatial cell-cell communications. The modeling framework of stMLnet encompasses two scales (i.e., intercellular scale and intracellular scale) and four layers (i.e., ligand-receptor-TF-target).

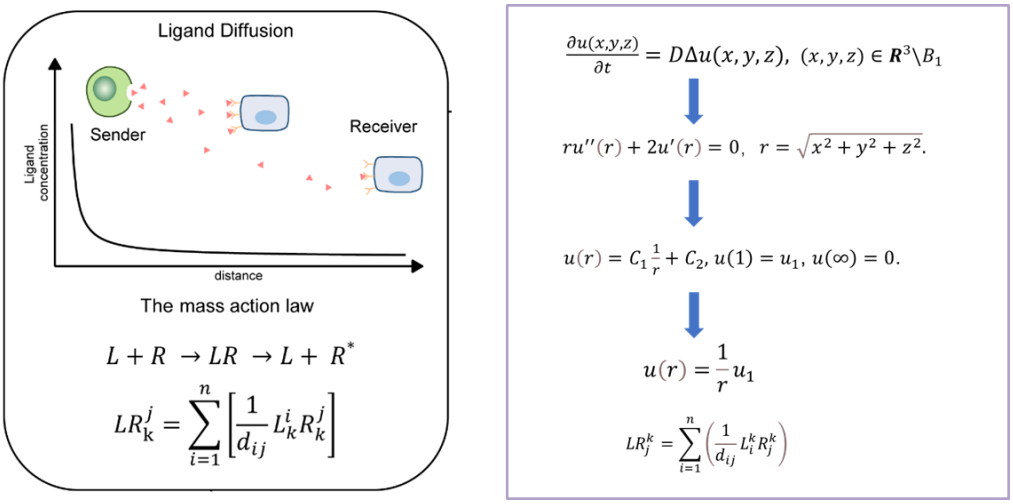

Figure S28. Model reduction and solving. stMLnet employs an effective model reduction and solving approach, yielding a parameter-free formula for spatially-dependent ligand-receptor signaling, significantly reducing the model complexity.

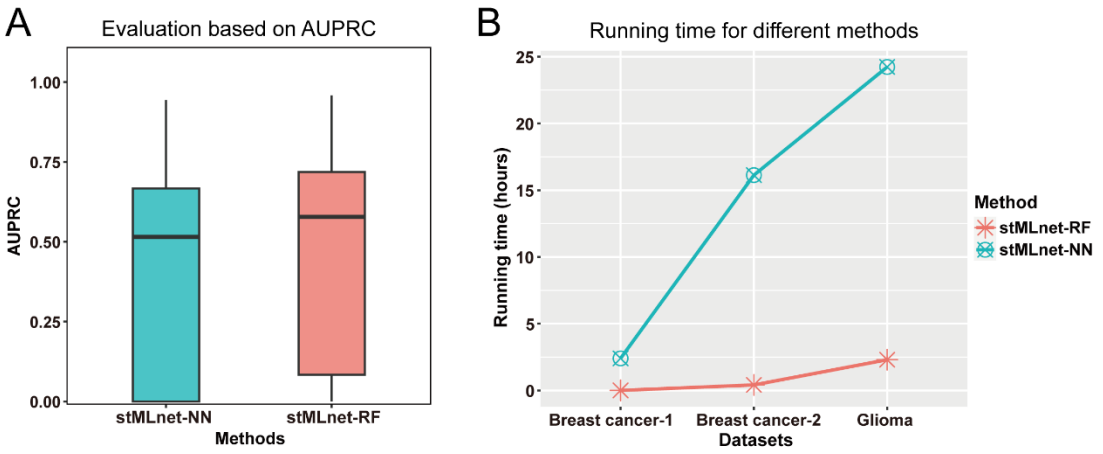

Figure S29. Performance comparison of using neural network regression and random forest regression to calculate LR importance score in stMLnet. (A) Performance evaluation of stMLnet with neural network regression (stMLnet-NN) and stMLnet with random forest regression (stMLnet-RF) using AUPRC metric. (B) Comparison of the running time (hours) of stMLnet-NN and stMLnet-RF on the three datasets.

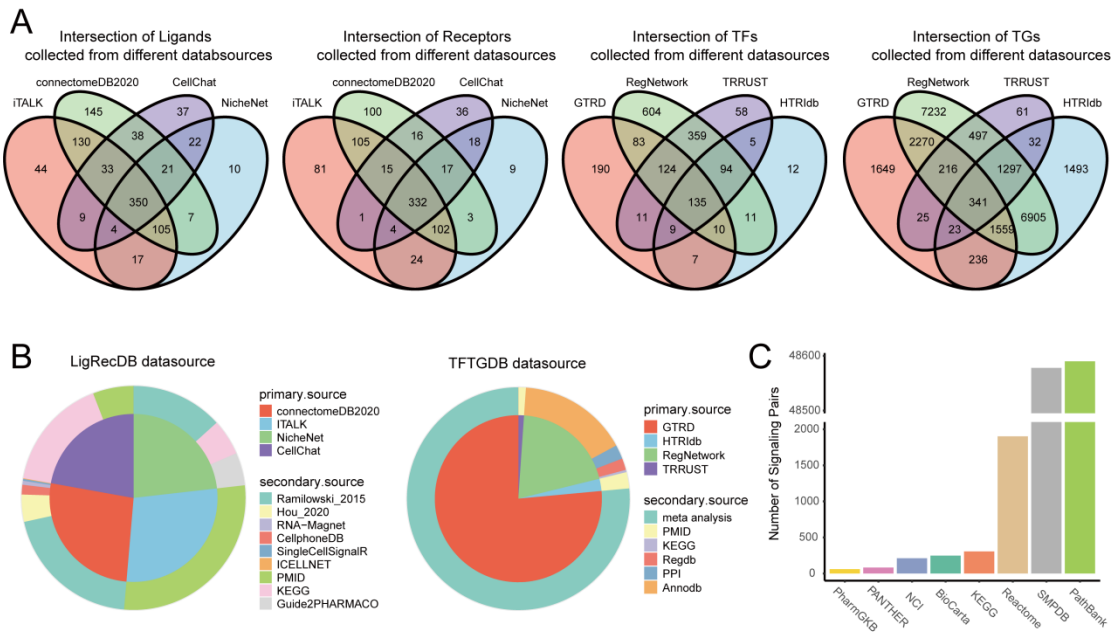

Figure S30. **The collection and sorting of prior knowledge database**. (**A**) The distribution of different types of molecules (ligands, receptors, TFs, and target genes) recorded in LigRecDB and TFTGDB prior databases. (**B**) The distribution of different types of interactions (LR pairs or TF-TG pairs) collected in LigRecDB and TFTGDB prior databases. (**C**) Numbers of molecular interactions within signaling pathways collected in different pathway databases.

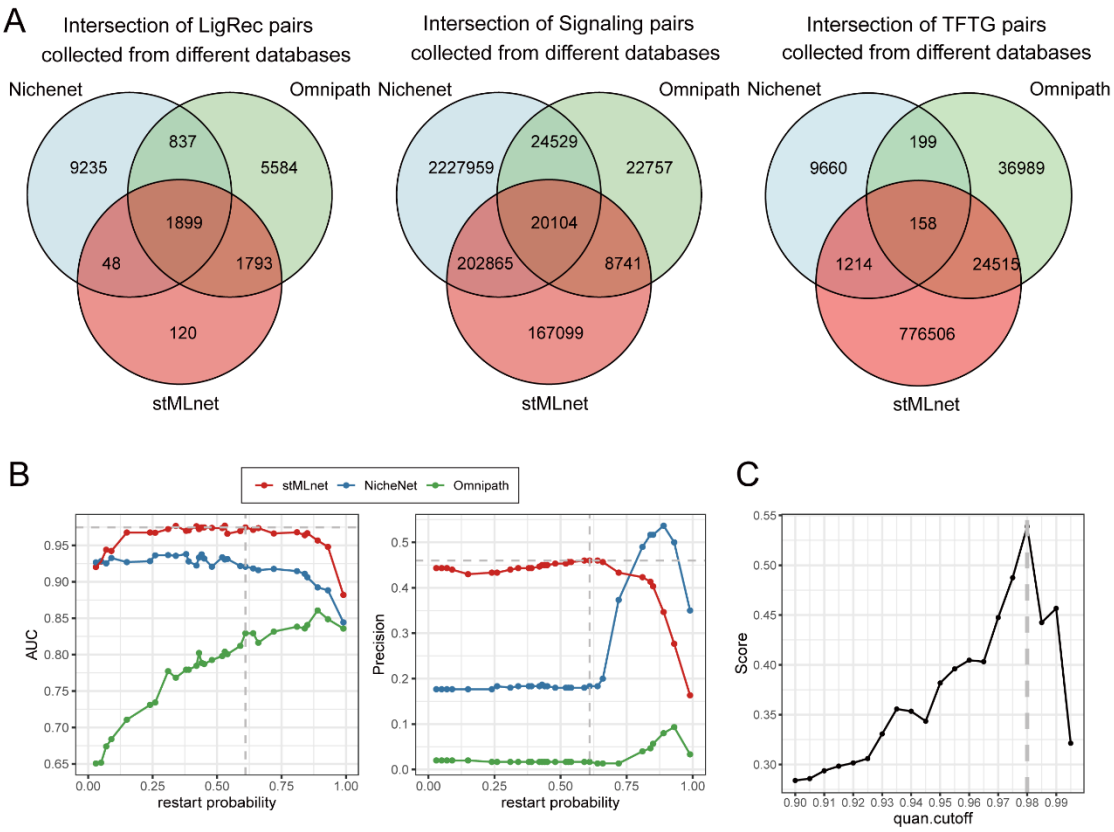

Figure S31. **Comparison and parameterization of prior knowledge databases**. (**A**) Comparison of interaction pairs (LR, signaling pairs and TF-TG) in stMLnet, NicheNet and Omnipath. (**B**) Cross-validation and random sub-sampling validation to determine the value of restart parameter of the random walk algorithm based on AUC and Precision metrics. stMLnet was compared with NicheNet and Omnipath. (**C**) Determining significant receptor-TF links from RecTF matrix using 129 sets of cell line expression data with various stimulations or perturbations. The values in RecTF matrix represent predicted probabilities of interactions between the upstream receptors and downstream TFs. An optimal quan.cutoff value was selected to determine significant receptor-TF links that maximizes the Score in the y axis, which is an index measuring both sparsity of RecTF matrix and information preservation in the cell line datasets.

Supplementary References

Andersen P, Morris R, Amaral D, Bliss T, O'Keefe J. 2006. The Hippocampus Book. *Oxford Neuroscience Series, New York*.

Andersson A, Bergenstrahle J, Asp M, Bergenstrahle L, Jurek A, Fernandez Navarro J, Lundeberg J. 2020. Single-cell and spatial transcriptomics enables probabilistic inference of cell type topography. *Commun Biol* **3**: 565.

Baccin C, Al-Sabah J, Velten L, Helbling PM, Grünschläger F, Hernández-Malmierca P, Nombela-Arrieta C, Steinmetz LM, Trumpp A, Haas S. 2020. Combined single-cell and spatial transcriptomics reveal the molecular, cellular and spatial bone marrow niche organization. *Nat Cell Bio* **22**: 38-48.

Bovolenta LA, Acencio ML, Lemke N. 2012. HTRIdb: an open-access database for experimentally verified human transcriptional regulation interactions. *BMC Genomics* **13**: 405.

Brin S, Page L. 1998a. The anatomy of a large-scale hypertextual Web search engine. *Computer Networks and ISDN Systems* **30**: 107-117.

Brin S, Page L. 1998b. The anatomy of a large-scale hypertextual Web search engine. *Computer Networks and ISDN Systems* **30**: 107-117.

Browaeys R, Saelens W, Saeys Y. 2020. NicheNet: modeling intercellular communication by linking ligands to target genes. *Nat Methods* **17**: 159-162.

Cabello-Aguilar S, Alame M, Kon-Sun-Tack F, Fau C, Lacroix M, Colinge J. 2020. SingleCellSignalR: inference of intercellular networks from single-cell transcriptomics. *Nucleic Acids Research* **48**: e55.

Cable DM, Murray E, Zou LS, Goeva A, Macosko EZ, Chen F, Irizarry RA. 2022. Robust decomposition of cell type mixtures in spatial transcriptomics. *Nat Biotechnol* **40**: 517–526.

Chen A, Liao S, Cheng M, Ma K, Wu L, Lai Y, Qiu X, Yang J, Xu J, Hao S et al. 2022. Spatiotemporal transcriptomic atlas of mouse organogenesis using DNA nanoball-patterned arrays. *Cell* **185**: 1777-1792.e1721.

Dries R, Zhu Q, Dong R, Eng CHL, Li HP, Liu K, Fu YT, Zhao TX, Sarkar A, Bao F et al. 2021. Giotto: a toolbox for integrative analysis and visualization of spatial expression data. *Genome Biol* **22**: 78.

E M, Ritchie, Phipson B, Wu D, Hu Y, Law CW, Shi W, Smyth GK. 2015. limma powers differential expression analyses for RNA-sequencing and microarray studies. *Nucleic Acids Research* **43**: e47.

Efremova M, Vento-Tormo M, Teichmann SA, Vento-Tormo R. 2020. CellPhoneDB: inferring cell-cell communication from combined expression of multi-subunit ligand-receptor complexes. *Nat Protoc* **15**: 1484-1506.

Eng C-HL, Lawson M, Zhu Q, Dries R, Koulena N, Takei Y, Yun J, Cronin C, Karp C, Yuan G-C et al. 2019. Transcriptome-scale super-resolved imaging in tissues by RNA seqFISH+. *Nature* **568**: 235-239.

Gracia Villacampa E, Larsson L, Mirzazadeh R, Kvastad L, Andersson A, Mollbrink A, Kokaraki G, Monteil V, Schultz N, Appelberg KS et al. 2021. Genome-wide spatial expression profiling in formalin-fixed tissues. *Cell Genomics* **1**: 100065.

H. T, C. F, J. P. 2006. Fast Random Walk with Restart and Its Applications. In *Sixth International Conference on Data Mining (ICDM'06)*, doi:10.1109/icdm.2006.70, pp. 613-622.

Han H, Cho JW, Lee S, Yun A, Kim H, Bae D, Yang S, Kim CY, Lee M, Kim E et al. 2018. TRRUST v2: an expanded reference database of human and mouse transcriptional regulatory interactions. *Nucleic Acids Res* **46**: D380-D386.

Hao Y, Hao S, Andersen-Nissen E, III WMM, Zheng S, Butler A, Lee MJ, Wilk AJ, Darby C, Zagar M et al. 2021. Integrated analysis of multimodal single-cell data. *Cell* **184**: 3573-3587.e3529.

Hou R, Denisenko E, Ong HT, Ramilowski JA, Forrest ARR. 2020. Predicting cell-to-cell communication networks using NATMI. *Nat Commun* **11**: 5011.

Huynh-Thu VA, Irrthum A, Wehenkel L, Geurts P. 2010. Inferring regulatory networks from expression data using tree-based methods. *PLoS One* **5**.

Jin S, Guerrero-Juarez CF, Zhang L, Chang I, Ramos R, Kuan CH, Myung P, Plikus MV, Nie Q. 2021. Inference and analysis of cell-cell communication using CellChat. *Nat Commun* **12**: 1088.

Karaayvaz M, Cristea S, Gillespie SM, Patel AP, Mylvaganam R, Luo CC, Specht MC, Bernstein BE, Michor F, Ellisen LW. 2018. Unravelling subclonal heterogeneity and aggressive disease states in TNBC through single-cell RNA-seq. *Nat Commun* **9**: 3588.

Kolmykov S, Yevshin I, Kulyashov M, Sharipov R, Kondrakhin Y, Makeev VJ, Kulakovskiy IV, Kel A, Kolpakov F. 2021. GTRD: an integrated view of transcription regulation. *Nucleic Acids Res* **49**: D104-D111.

Li H, Ma T, Hao M, Guo W, Gu J, Zhang X, Wei L. 2023. Decoding functional cell-cell communication events by multi-view graph learning on spatial transcriptomics. *Brief Bioinform* **24**: bbad359.

Li Y, Xu J, Liu Y, Zhu J, Liu N, Zeng W, Huang N, Rasch MJ, Jiang H, Gu X et al. 2017. A distinct entorhinal cortex to hippocampal CA1 direct circuit for olfactory associative learning. *Nat Neurosci* **20**: 559-570.

Linderman GC, Zhao J, Roulis M, Bielecki P, Flavell RA, Nadler B, Kluger Y. 2022. Zero-preserving imputation of single-cell RNA-seq data. *Nat Commun* **13**.

Liu ZP, Wu C, Miao H, Wu H. 2015. RegNetwork: an integrated database of transcriptional and post-transcriptional regulatory networks in human and mouse. *Database (Oxford)* **2015**: bav095.

Lü L, Zhou T. 2011. Link prediction in complex networks: A survey. *Physica A: Statistical Mechanics and its Applications* **390**: 1150-1170.

Moffitt JR, Bambah-Mukku D, Eichhorn SW, Vaughn E, Shekhar K, Perez JD, Rubinstein ND, Hao J, Regev A, Dulac C et al. 2018a. Molecular, spatial, and functional single-cell profiling of the hypothalamic preoptic region. **362**: eaau5324.

Moffitt JR, Bambah-Mukku D, Eichhorn SW, Vaughn E, Shekhar K, Perez JD, Rubinstein ND, Hao J, Regev A, Dulac C et al. 2018b. Molecular, spatial, and functional single-cell profiling of the hypothalamic preoptic region. *Science* **362**: eaau5324.

Noel F, Massenet-Regad L, Carmi-Levy I, Cappuccio A, Grandclaudon M, Trichot C, Kieffer Y, Mechta-Grigoriou F, Soumelis V. 2021. Dissection of intercellular communication using the transcriptome-based framework ICELLNET. *Nat Commun* **12**: 1089.

Quail DF, Bowman RL, Akkari L, Quick ML, Schuhmacher AJ, Huse JT, Holland EC, Sutton JC, Joyce JA. 2016. The tumor microenvironment underlies acquired resistance to CSF-1R inhibition in gliomas. *Science* **352**: aad3018.

Ramilowski JA, Goldberg T, Harshbarger J, Kloppmann E, Lizio M, Satagopam VP, Itoh M, Kawaji H, Carninci P, Rost B et al. 2015. A draft network of ligand–receptor-mediated multicellular signalling in human. *Nat Commun* **6**: 7866.

Ravi VM, Will P, Kueckelhaus J, Sun N, Joseph K, Salié H, Vollmer L, Kuliesiute U, von Ehr J, Benotmane JK et al. 2022. Spatially resolved multi-omics deciphers bidirectional tumor-host interdependence in glioblastoma. *Cancer Cell* **40**: 639-655.e613.

Stickels RR, Murray E, Kumar P, Li J, Marshall JL, Di Bella DJ, Arlotta P, Macosko EZ, Chen F. 2021. Highly sensitive spatial transcriptomics at near-cellular resolution with Slide-seqV2. *Nat Biotechnol* **39**:

313-319.

Stuart T, Butler A, Hoffman P, Hafemeister C, Papalexi E, Mauck WM, Hao Y, Stoeckius M, Smibert P, Satija R. 2019. Comprehensive Integration of Single-Cell Data. *Cell* **177**: 1888-1902.e1821.

Tong H, Faloutsos C, Pan J-y. 2006. Fast Random Walk with Restart and Its Applications. *Sixth International Conference on Data Mining (ICDM'06), Hong Kong, China* doi:10.1109/ICDM.2006.70: 613-622.

Travaglini KJ, Nabhan AN, Penland L, Sinha R, Gillich A, Sit RV, Chang S, Conley SD, Mori Y, Seita J et al. 2020. A molecular cell atlas of the human lung from single-cell RNA sequencing. *Nature* **587**: 619-625.

van Strien NM, Cappaert NL, Witter MP. 2009. The anatomy of memory: an interactive overview of the parahippocampal-hippocampal network. *Nat Rev Neurosci* **10**: 272-282.

Wang Y, Wang R, Zhang S, Song S, Jiang C, Han G, Wang M, Ajani J, Futreal A, Wang L. 2019. iTALK: an R Package to Characterize and Illustrate Intercellular Communication. *bioRxiv* doi:10.1101/507871.

Wu SZ, Al-Eryani G, Roden DL, Junankar S, Harvey K, Andersson A, Thennavan A, Wang CF, Torpy JR, Bartonicek N et al. 2021. A single-cell and spatially resolved atlas of human breast cancers. *Nat Genet* **53**: 1334-1347.